Direct numerical simulation of a supersonic turbulent boundary layer subjected to a concave surface

Xiaoshuai Wu, Jianhan Liang,[*] and Yuxin Zhao
*Science and Technology on Scramjet Laboratory, National University of Defense Technology,
Changsha 410073, China*

Direct numerical simulation is performed to investigate the flow physics of a supersonic turbulent boundary layer subjected to a longitudinal concave surface. Two physically consistent approaches are exploited to determine the boundary layer edge, and it is found that this turbulent boundary layer becomes noticeably thinned on the concave surface, which reflects the pronounced role of rise in density during this flow compression. In general the boundary layer is highly distorted, as manifested by wall pressure properties. Examinations of velocity statistics reveal that the scaling well established in canonical turbulence is violated in this distorted case. Mean streamwise velocity neither conforms to the universal log law nor obeys the velocity-defect law. Considerable increase is observed for Reynolds stresses throughout the concave surface, pointing to the effect of turbulence amplification. Nevertheless, the stress-bearing turbulent motions have barely changed in character, as evidenced by the quadrant analysis and structure parameter. The turbulence amplification is then understood by inspecting the production term of turbulent kinetic energy. We demonstrate that the outer boundary layer holds an increasingly important contribution to the total turbulence production throughout the concave surface. Accordingly, the amplification of turbulent kinetic energy is prominent in the outer layer. More insights are provided by inspecting the energy spectra. We find the outer-layer large structures are highly energized, even with an energy peak appearing in the lower-wake region, and they superimpose substantial large-scale energies on the near-wall region. Structural analyses demonstrate the organized turbulent motions, which are well scaled in canonical turbulence, have generally changed in their characteristic lengthscales under the influence of concave surface. Importantly, the flow visualization reveals stronger footprints overlaid onto the near-wall region, which suggests enhanced inner-outer interactions. This perspective, aided by the spanwise two-point correlations, is moreover supported by the quantification of amplitude modulation through a mathematical diagnostic tool. Results demonstrate that turbulence modulation is still governed by log-region superstructures, whereas the modulation strength has noticeably increased throughout the concave surface.

I. INTRODUCTION

The design of high-speed vehicles has invigorated fundamental researches on compressible turbulent boundary layers (TBLs). Lots of endeavors [1–4] have been devoted to the canonical cases (i.e., without external perturbations), and they collectively point to the perspective that supersonic turbulence possesses a general similarity with the incompressible counterpart since principal differences between two flow regimes can be scaled out by mean density variations

---

*jhleon@vip.sina.com

following Morkovin's hypothesis [5–6]. Nevertheless, more prevalent in practice are perturbed flows over various curved geometries (e.g., scramjet intake). Such curved surfaces can bring about intense turbulence distortions and hence lead to quite complicated operating conditions for vehicles. Therefore understanding the potential physics is significant for effective flow control methodologies as well as for novel hypersonic vehicle designs. Despite some experimental studies available in literature, a profound understanding regarding the concave surface remains lacking.

The first investigation on curved wall surfaces dates back to the period when Ludwig Prandtl had just set up the foundations of boundary layer theory (see Ref. [7]). Later, it was the remarkable work by Bradshaw [8] that provided a framework to classify these effects into different kinds of extra strain rates e, e.g., strain rates associated with streamline curvature ($\partial V/\partial x$), bulk compression ($\nabla \cdot \boldsymbol{U}$), and so on. Despite existing studies in the incompressible case, investigations directly conducted in the supersonic regime are in practice mandatory to understand the involved extra strain rates, because an incompressible analogy is not readily available owing to the unique character of supersonic flow (density changes more rapidly than velocity as pressure varies) [6]. Generally for supersonic flows, concave streamline curvature, bulk compression, and adverse pressure gradient (APG) belong to destabilizing extra strain rates [9,10], since the conservation of angular momentum leads to the increase in spanwise vorticity due to the reduction of cross-sectional area in the wall-normal-streamwise plane [11]. The opposite is true for the counterparts of the extra strain rates. In practical configurations, it is very likely that more than one kind of perturbations occur simultaneously. For instance, the supersonic flow subjected to a longitudinal concave surface undergoes the combined destabilization effects of concave streamline curvature, bulk compression, and APG. In contrast to interests in understanding separate contributions of each extra strain rate (e.g., Ref. [10]), the present paper focuses on the combined effects related to the concave wall surface, which is practically valuable since the overall effects cannot be predicted by a simple summation of their separate components (the involved extra strain rates interact nonlinearly) [12].

To date the effects of longitudinal concave surface on supersonic TBLs have been understood mostly through experiments. It is clear that, contrary to the incompressible case [13], the concave surface in supersonic flows generally leads to thinned boundary layer and increased wall-shear stress (e.g., Refs. [14,15]), since the increase in density overrides the decrease in velocity beyond low Mach number and the stream tubes are compressed [6]. The mean velocity property with concave surface has been frequently discussed, and it is revealed that the van Driest transformed streamwise velocity is characterized by a dip below the universal log law [16–18]. The physics underlying this feature of a dip are that the lengthscales of turbulent motions increase more rapidly in the perturbed turbulence than in the canonical case [8], as further evidenced by the observation that the most energetic motions in the near-wall region shift towards lower frequency [17]. Interestingly, it was revealed that this dip is directly linked to the presence of streamline curvature, relatively irrelevant to APG [19]. Exceptions, however, to the appearance of a dip over the concave wall exist in literature [20]. Another prominent influence of the concave surface is to amplify turbulence intensities across the whole layer [17–18], and this amplification is most striking in the outer region since extra strain rates have their strongest relative effect due to the continuous decrease in principal shear $\partial U/\partial y$ away from the wall [12]. It is stemming from an assumption of rapid perturbation that the influences of extra strain rates e can be evaluated by the total impulse $I = \int e\,dt$ [6]. It was revealed that the perturbation strength, if strong enough, can notably alter the structure angle and lengthscales of organized turbulent motions [16]. Nevertheless, the perturbation rate, i.e., the path taken by perturbation, does play its role. For example, turbulent structures would remain essentially unaltered if the perturbation rate is slow enough to permit readjustment of the turbulence to new boundary conditions [17]. Despite in-depth understanding gained from the above-cited work, an experimental scope is sometimes restricted due to the measuring difficulties in supersonic regimes. For instance, up to 15% uncertainty is commonly encountered in determining the wall-shear stress [21].

Contrasting with the early experiments, there currently are few studies making the best of direct numerical simulation (DNS) in accurately predicting such distorted turbulence, and we are therefore

motivated to make one contribution of this kind. Particularly, DNS provides direct access to detailed three-dimensional flow fields, and facilitates investigations of turbulent organized motions, in light of the newly discovered flow phenomena within the last two decades or so [22–24]. The current understanding of wall turbulence has unveiled a self-sustaining near-wall cycle based on insightful low-Reynolds-number simulations [25,26], and has also highlighted a new type of outer-scaled organized structures, termed very large-scale motions [27] or superstructures [28]. Importantly, there exist intense interactions between the near-wall cycle and superstructures [29,30], the study of which is important not only for modeling near-wall statistics [31,32] but also for drag reduction strategies [33,34]. Nevertheless, the relevant issues are not well addressed in the distorted cases. The questions that then emerge are how the organized motions respond and whether the inner-outer interactions are influenced by curved wall surface.

In this paper, numerical simulations have been conducted to investigate a supersonic turbulent boundary layer subjected to a longitudinal concave surface. A relatively complete document is provided regarding the turbulence statistics and organized motions. Particular attentions have been paid to the turbulence amplification as well as inner-outer interactions. For clarity, when mentioning the influence of concave surface in the following, we are referring to the combined effects, which comprise the contributions from concave streamline curvature, bulk compression, and adverse pressure gradients. The paper is organized as follows. In Sec. II the simulation approach is briefly introduced, together with the assessment of DNS databases. The basic statistics are given in Sec. III A. Flow organizations are investigated in Sec. III B, followed by the analysis of nonlinear inner-outer interaction in Sec. III C. Finally, concluding remarks are given in Sec. IV.

II. DIRECT NUMERICAL SIMULATION

A. Numerical strategy

In the present simulation, the governing equations are the three-dimensional Navier-Stokes equations in the conservative form for a perfect gas, which are solved in the curvilinear coordinate by using a transformation from the Cartesian physical space to the computational space. The viscous stress tensor is computed by adopting the constitutive relations for a Newtonian fluid, and the heat flux vector is calculated through Fourier's law of heat conduction. The molecular viscosity μ is assumed to obey Sutherland's law, and the thermal conductivity is given by $k = \mu c_p / \Pr$, with the molecular Prandtl number being 0.72. Finite differences are employed to discretize the governing equations. The flow solver [35–36] relies on the WENO-SYMBO scheme [37] to compute the inviscid terms with Steger-Warming flux splitting, and utilizes an eighth-order central scheme to calculate the viscous terms. Third-order TVD (total variation diminishing) Runge-Kutta method is implemented for time advancement.

As sketched in Fig. 1, the present flow configuration mimics the Model II devised by Jayaram *et al.* [17] but with a lower reference Reynolds number (i.e., $\mathrm{Re}_{\theta,\mathrm{ref}} = 2920$ in our DNS). Note that the experimental Reynolds number (i.e., $\mathrm{Re}_\theta \approx 8 \times 10^4$) is too high to be afforded by DNS nowadays. It then follows that comparisons with the experiment are meaningful when the outer coordinate is employed, based on the assumption that outer-scaled statistics of TBL are insensitive to Reynolds number. We also note that the rest flow conditions are identical to the experiment, such as the free-stream temperature, Mach number, thermal wall condition, and concave surface curvature. To be specific, the upstream flow conditions are $T_\infty = 102$ K and $M_\infty = 2.87$. An isothermal boundary is adopted here by setting the wall temperature as the nominal adiabatic value $T_{aw}/T_\infty = 1 + r(\gamma - 1)/2M_\infty^2$, with the recovery factor being $r = \Pr^{1/3}$. A laminar solution is prescribed as the inflow condition, and a tripping scheme [2] is exerted slightly downstream to establish the turbulent state. A long distance is adopted here to allow for boundary layer transition and post-transitional effect fading. One streamwise location in the fully turbulent regime (i.e., $L1$) is taken as the reference incoming flow for the downstream concave surface, which is characterized
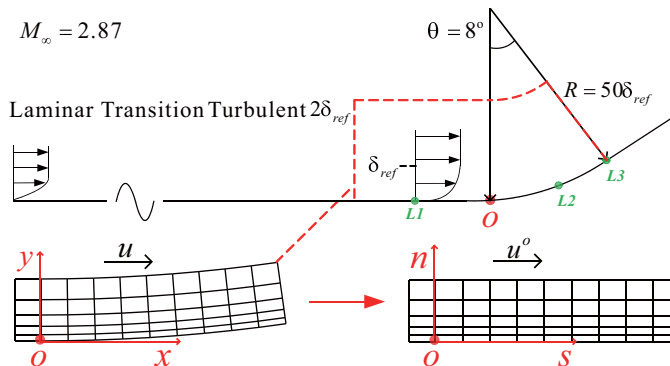
FIG. 1. A sketch of the flow configuration. The bottom shows the velocity projection from the Cartesian coordinates to the orthogonal coordinates.

by a turning angle of $8°$ and radius of $50\delta_{\text{ref}}$ (δ_{ref} being reference boundary layer thickness). This means that the supersonic turbulent boundary layer will experience the perturbation impulses of $I_p = 0.41$ (from bulk compression) and $I_\theta = 0.14$ (from streamline curvature) over a distance of $7\delta_{\text{ref}}$, and develop into a nonequilibrium state during distortion. Downstream from the curved region, the turbulent boundary layer starts relaxation on the following flat plate. Presently, it is our main aim to investigate the distortion stage. The stage of relaxation, which requires rather long distance to cover its full process, is left for future study (as discussed in Sec. III A). In the present paper, analyses have been conducted by comparing three typical streamwise locations, i.e., the reference location $L1$, midpoint $L2$, and end $L3$ of the concave surface. Accordingly, the statistics are collected in the interested domain (with a height of $2\delta_{\text{ref}}$) encircled by the dotted line in the sketch, which is devised carefully to guarantee sufficient mesh resolutions for the enclosed turbulence. For meaningful representations of the flow physics, an orthogonal coordinate system originated at the onset of the curvature is introduced here, in which s denotes the streamwise distance parallel with the model surface and n refers to the distance normal to the wall. The orthogonal coordinates facilitate the projection and decomposition of velocities over the curved surface, as adopted by previous studies [7,17]. It is worth noting that the axis s roughly matches the local streamlines [as shown in Fig. 3(a)] if neglecting the influence of flow tube compression, and the resulting velocity fluctuations are endowed with a clear physical meaning, as will be discussed in Sec. III A.

A side view of the sample grid is depicted in Fig. 2. The computational domain is bounded by the laminar inflow, isothermal wall boundary, and nonreflecting top and outflow boundaries. Periodicity is prescribed in the spanwise direction. A testing simulation (case 1) was conducted in advance for determining the computational domain, grid resolution, and distribution; the resulting statistics turn out to be in good agreement with the well-accepted literature data (as discussed below), which verifies the proper numerical setup. For improved resolution of the turbulent structures, a refined mesh grid (case 2) is adopted for the present paper. Parameters of two cases are summarized in Table I. The domain height is much larger than the boundary layer thickness; however, the grid points in the wall-normal direction are clustered near the wall to fully resolve the turbulent flow, with 120 points (for case 2) located within the interested domain. The domain width, set as $3\delta_{\text{ref}}$, is wide enough to sufficiently accommodate the turbulence dynamics; this is posteriorly validated by the decaying of spanwise two-point correlations at the tails (see Figs. 14 and 16). The concave surface is followed by a short flat plate of $7\delta_{\text{ref}}$. A fringe region with coarsened mesh resolutions is moreover attached at the outflow boundary, for the purpose of further damping the possible disturbance reflections towards the domain inside. Throughout the paper, u, v, and w denote the velocity components in the x, y, and z directions in the Cartesian coordinates, and the superscript "o" (e.g., u^o) denotes the velocity projected onto the orthogonal coordinates. Following the standard
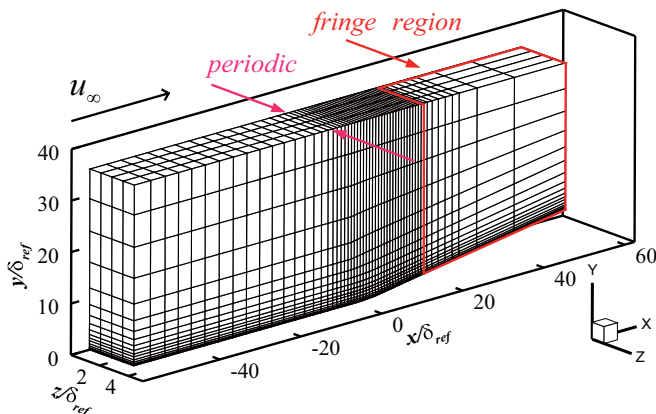
FIG. 2. A sample grid for the direct numerical simulation.

Reynolds decomposition ($f = \overline{f} + f'$), the overbar or capitalized variable denotes the temporal mean, and the prime symbol refers to the fluctuating component. The Favre decomposition is then denoted as $f = \tilde{f} + f''$, where $\tilde{f} = \overline{\rho f}/\overline{\rho}$.

B. Assessment of the DNS data

Before the collection of statistics, a washout time of seven eddy turnovers (i.e., $7\delta_{\text{ref}}/u_\tau$ measured at the reference location) was initially discarded from the simulation, which sufficiently allows for the TBL to be arranged onto a statistically stationary state. Equally spaced time samples are collected at the selected locations $L1$–$L3$ spanning a total time period of $\Delta T_s \approx 15\delta_{\text{ref}}/u_\tau$, which is comparable to the well-accepted DNS (e.g., Ref. [38]). As an aside, we have confirmed that this sampling period is long enough to guarantee that our results reported below are sufficiently converged, although the details are omitted here. The datasets of simulation case 2 are assessed in the following, and the testing case 1 is included for checking grid sensitivity.

For a visual impression, Fig. 3 depicts one snapshot in the (x, y) plane, with the fringe region being omitted. As can be seen, transition commences shortly downstream from the tripping location and the boundary layer quickly becomes turbulent with the striking appearance of large-scale bulges in the outer region. The turbulent boundary layer develops naturally into high Reynolds number under zero-pressure gradient (ZPG) until affected by the concave surface, over which the flow deflects with the formation of an oblique shock far outside the boundary layer. It should be noted that this flow configuration was deliberately devised by Jayaram et $al.$ [17] to avoid the influence of shock on the turbulent boundary layer. This point can be easily checked by examining the mean

TABLE I. Summary of parameters. Re_θ shows the Reynolds numbers covered by the DNS. L_x, L_y, and L_z are the box dimensions along three axes; N_x, N_y, and N_z are the grid sizes. The mesh resolutions (Δ values) are only reported for the interested domain. The superscript $+$ refers to quantity made nondimensional with the friction velocity $u_\tau = (\tau_w/\rho_w)^{1/2}$ and viscous length scale $\delta_v = v_w/u_\tau$. The mesh spacing in wall-normal direction is reported at the boundary layer edge (Δy_δ^+), while the value at the wall (Δy_w^+) is kept no larger than 1.

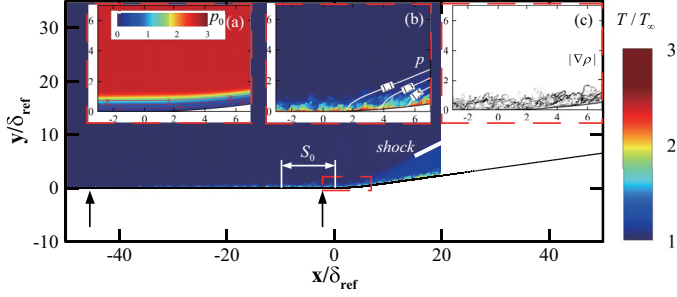| Case	Re_θ	$(L_x, L_y, L_z)/\delta_{\text{ref}}$	N_x, N_y, N_z	Δx^+	Δy_δ^+	Δz^+
1	$550-3900$	$106 \times 35 \times 3$	$2700 \times 100 \times 256$	$8-13$	$18-25$	$4.5-6.5$
2	$550-3900$	$106 \times 35 \times 3$	$2900 \times 140 \times 320$	$6-10$	$10-15$	$3.5-5.5$

FIG. 3. A snapshot colored by temperature. Shock (thick white line) forms well above the boundary layer. The turbulence gets organized after tripping (left arrow), and provides a region of equilibrium ZPG state (of the streamwise length $s_0 \approx 10\delta_{ref}$), where one station (right arrow) is adopted as the reference TBL for the downstream concave region. Subfigures are the enlarged portion of the concave region (dashed box) and show streamlines overlaid on total pressure contour $p_0/(\rho_\infty u_\infty^2)$ (a), mean pressure isolines p/p_∞ overlaid on temperature contour (b), and instantaneous numerical Schlieren $|\nabla\rho|\delta/\rho_\infty$(c).

pressure property depicted in plot (b). One can notice that there is no intersection of mean pressure isolines (within the enlarged scope), and thus the average flow is without the presence of shock inside the boundary layer. By inspecting the numerical Schlieren in plot (c), we note that the shock wave is as well absent in the instantaneous flow fields. Actually, the shock is formed well above the boundary layer, roughly at a wall-normal height of 6δ. To put it briefly, the inviscid flow passing right above the boundary layer experiences isentropic compression. As an aside, reflected by the numerical Schlieren are the large-scale bulges residing in the outer boundary layer, the backs and fronts of which are featured by large density gradients.

As mentioned previously, the numerical setup is devised with caution to produce an equilibrium turbulent boundary layer upstream from the concave surface. One effective approach to quantify the turbulent state developed from artificial techniques is by examining the skin friction coefficient $C_f = 2\bar{\tau}_w/(\rho_\infty u_\infty^2)$, as commonly done in literature [38–40]. In detail, the onset of turbulence from the artificial perturbations is marked by an overshoot of skin friction at the late stage of transition [2], and a fully developed state is achieved when the post-transitional effect fades, with the skin friction collapsed onto the equilibrium correlation. For assessment of the reference location $L1$, we examine the skin friction coefficient according to the van Driest II theory [41,42] with the following transformation:

$$C_{fi} = F_c C_f, \quad \mathrm{Re}_{\theta i} = \mu_\infty/\mu_w \mathrm{Re}_\theta \tag{1}$$

where

$$F_c = \frac{T_w/T_\infty - 1}{\arcsin^2\alpha}, \quad \alpha = \frac{T_w/T_\infty - 1}{\sqrt{T_w/T_\infty(T_w/T_\infty - 1)}}. \tag{2}$$

It turns out that the reference TBL is characterized by a momentum Reynolds number $\mathrm{Re}_{\theta i} = 1280$ (with $\mathrm{Re}_\theta = 2920$) and skin friction $C_{fi} = 4.09 \times 10^{-3}$, which means the transformed skin friction falls within 2% uncertainty with the incompressible empirical correlation $C_{fi} = 0.024\mathrm{Re}_{\theta i}^{(-1/4)}$ [43]. This discrepancy is actually negligible and lies within the 5% tolerance adopted by Schlatter and Örlü [40] in assessing the published high-quality DNS datasets. Thus the present simulation is reliable. It is also worth noting that a region of equilibrium ZPG TBL (of the distance $s_0 \approx 10\delta_{ref}$) is available upstream from the concave surface (see Fig. 3), where the transformed skin friction remains within 2% uncertainty with the empirical correlation.
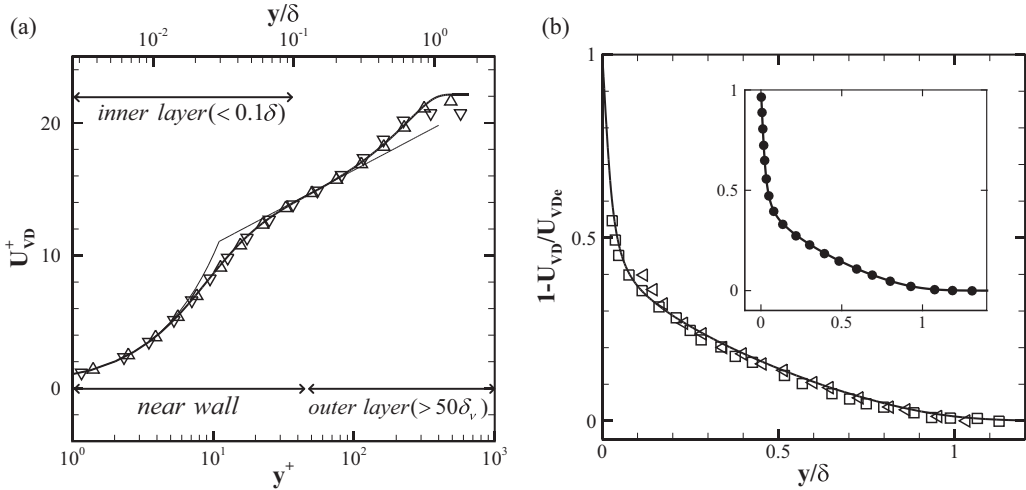
FIG. 4. (a) The van Driest transformed velocity at the reference location with $Re_\tau = 375$. Symbols denote DNS data by Pirozzoli and Bernardini [44] at $Re_\tau = 250$ (upside-down triangles) and Schlatter and Örlü [40] at $Re_\tau = 360$ (triangles). Thin lines denote the linear and logarithmic regions by $U_{VD}^+ = y^+$ and $U_{VD}^+ = 1/0.41 \log(y^+) + 5.2$, respectively. (b) The mean defect velocity, compared with experimental data by Bookey *et al.* [45] (left triangles) and Piponniau *et al.* [46] (squares). The inset compares the simulation case 2 (line) with case 1 (solid circles).

We continue to assess the velocity evolvement at the reference location. Since the turbulent boundary layer possesses different speeds in convergence from transition to an equilibrium state (the outer layer has relatively slower convergence than the inner layer [39]), the assessment is here conducted separately regarding the inner and outer layers, as shown in Fig. 4. As an aside, the bounds of two layers are adopted following Pope [47]. To check the inner-layer convergence, Fig. 4(a) shows the streamwise mean velocity, by using van Driest transformation ($dU_{VD} = (\bar{\rho}/\bar{\rho}_w)^{1/2}dU$). It can be seen that the van Driest transformed velocity follows the incompressible law of the wall very well, consistent with the notion of weak compressibility hypothesis [5]. Note that the logarithmic region is adopted here by a lower limit of $y^+ = 30$ and an upper bound of $y/\delta = 0.2$. The log-law distribution is connected with the attached eddy hypothesis [48], and its existence is universal in wall turbulence [49]. In the present paper, the log-law constants are found to be von Kármán constant $\kappa = 0.41$ and $C = 5.2$. To examine the outer-layer convergence, Fig. 4(b) depicts the mean defect velocity in outer units. The present result is in very good agreement with the supersonic experiments in the defect layer. This means that the upstream and history effects within the outer region are forgotten, and thus validates the present simulation. Furthermore, the inset of plot (b) includes the velocity from testing case 1 (solid circles). The observation that two velocity profiles collapse very well thus validates the adequacy of grid resolution of the present simulation (case 2). Briefly, converged results, which are independent of mesh resolutions, are achieved.

To further assess the development of small-scale structures in the inner layer, Fig. 5(a) depicts the root-mean-square (rms) vorticity fluctuations in wall units. The streamwise component shows a local minimum and maximum at $y^+ = 4$ and 17, respectively, which reflect the signature of an average streamwise vortex located at $y^+ = 17$ with a radius of $r^+ = 13$, consistent with the previous finding [50]. The vorticity fluctuations are closely related with the tilting and stretching effects by near-wall streaks, and hence play a significant role in the self-sustaining process of wall turbulence (see Refs. [51,52]). The present vorticity fluctuations exhibit excellent agreement with the supersonic DNS [44], indicating the underlying structures are accurately reproduced. To validate the flow convergence in the outer layer, Fig. 5(b) reports the distribution of streamwise Reynolds stress in the outer coordinate, and Morkovin's scaling [6] is employed for comparisons
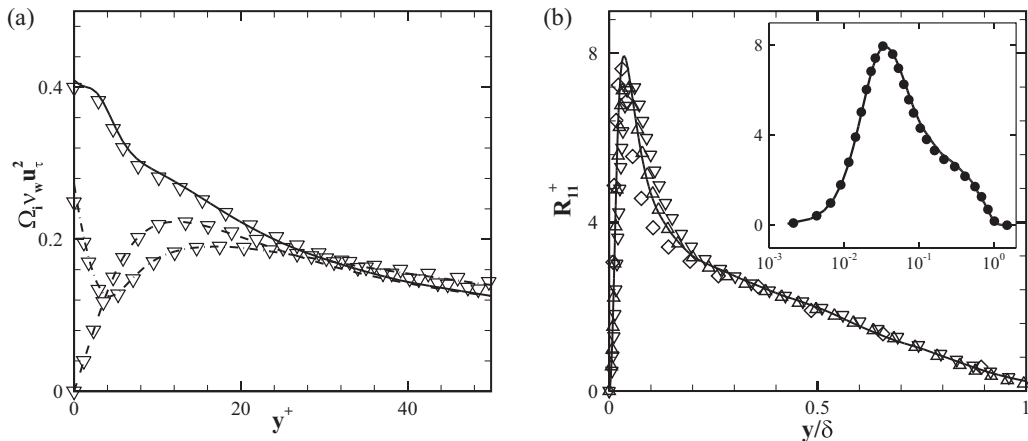
FIG. 5. (a) Distributions of rms vorticity fluctuations $\Omega_i = \overline{\omega_i'^2}^{1/2}$ for streamwise (dash-dotted), wall-normal (dashed), and spanwise components (solid). (b) Streamwise Reynolds normal stress, i.e., $R_{ij}^+ = (\bar{\rho}/\bar{\rho}_w)\overline{u_i'u_j'}/u_\tau^2$, in the outer coordinate. Triangles are DNS by Schlatter and Örlü [40] at $Re_\tau = 360$, and diamonds denote experiments by DeGraaff and Eaton [53]. Upside-down triangles denote the data by Pirozzoli and Bernardini [44] at $Re_\tau = 250$ in both (a) and (b). The inset compares datasets case 2 (line) with case 1 (solid circles).

with literature data of different flow conditions. The agreement is excellent (in the outer layer) with both the supersonic and incompressible data, meaning that the large-scale structures therein are of a genuine equilibrium state. The inset also includes the results obtained from datasets case 1 (solid circles). Very good collapse is observed across the whole layer, which verifies the present simulation (case 2) is free from the influence of grid resolutions.

Overall, it can be said that a generic turbulent boundary layer, free from post-transitional effect, is achieved upstream from the curved region, and thus allows for reliable quantification of the turbulence distortion. In the data validation and following investigations, available incompressible studies have been frequently cited to aid our analyses. This is because there exists a general similarity between the canonical incompressible and compressible turbulence under the hypothesis of weak compressibility [5,6], as validated by extensive endeavors (e.g., Refs. [1–4]). The good agreement with well-accepted literature data confirms that our simulation is one DNS of high quality and reliability.

III. RESULTS AND DISCUSSIONS

A. Basic statistics

The turbulent boundary layer would be severely distorted in the presence of a concave surface, and its development behaves differently from the canonical counterpart. A basic picture of the supersonic boundary layer response is given in this section. We investigate the distortion of the mean turbulent boundary layer and try to understand the turbulence amplification.

1. Boundary layer thickness and wall pressure

The determination of boundary layer edge in this kind of distorted flow deserves detailed discussions. According to the profound theory of boundary layer by Ludwig Prandtl, viscous effects would be confined to a thin layer along the (nonslip) solid surface for wall-bounded flows of (comparatively) high Reynolds numbers, and it is beyond this thin layer that the flow behaves like it is inviscid (see Ref. [54]). Such a thin region occupies only a small portion of the total flow field, but is responsible for significant momentum transfer or velocity gradient from the potential flow

to the wall. The underlying scenario is one whereby the fluid flow variable (say the streamwise velocity U) changes rapidly across the viscous region, and at the outer edge it achieves some value (say U_e), which is dependent on the incoming free stream (say U_∞) and the shape of the wall surface. It then follows that the boundary layer thickness can be practically determined as the position where the streamwise velocity reaches a certain percentage of the outer-edge value. For instance, in canonical flows the percentage 99% (and hence δ_{99}) is commonly adopted by the fluid community. This determination, however, is hardly suitable for the distorted flow, such as the one inspected here, because the inviscid supersonic flow is decelerated during the compression and the outer-edge velocity cannot be easily or precisely measured beforehand.

Nevertheless, one should keep in mind that the total pressure exhibits rapid increases across the viscous region [see Fig. 3(a)], and it theoretically remains unchanged in the upper inviscid region during this isentropic compression. It follows that the total pressure can be adopted for determining the boundary layer thickness (say δ). Herein we consider a normalized quantity (say p_0^*), which is defined as the ratio of the difference between the total pressure and wall pressure with respect to the free-stream value [18] or expressed as $p_0^* = (p_0 - p_w)/(p_{0,\infty} - p_{w,\infty})$. Normally, one would expect this normalized quantity approaches the unit beyond the viscous flow region. For plausible measurement of δ, imposing a threshold value (say th_{p_0}) is probably inevitable. Normally, a larger threshold value leads to a thicker measurement of the boundary layer. In the present paper, we aim to make the resulting thickness δ the quantitative analogy or best estimate of the traditional δ_{99}, otherwise it will be hard to include the investigations of canonical turbulence for meaningful comparisons. Specifically, we consider the upstream equilibrium ZPG region available in our simulation (see Fig. 3), where the definitions of both δ_{99} and δ are applicable, the thickness δ is calculated for different magnitude of th_{p_0} ranging from 0 to 1, and we compute the mean-square error (MSE) between the traditional δ_{99} and the resulting δ on this ZPG region, i.e., $\mathrm{MSE} = \int_{-1}^{0} (\delta - \delta_{99})^2 \, d(s/s_0)$ with the streamwise length being $s_0 \approx 10\delta_{\mathrm{ref}}$. To obtain the best estimate of δ_{99}, the mean-square error should be minimized by the threshold value, that is adopted for determining δ. Displayed in the inset of Fig. 6(a) is the mean-square error versus different magnitude of th_{p_0}. Indeed, a minimum appears at certain large magnitude. Accordingly, the threshold value is found to be $\mathrm{th}_{p_0} \approx 0.86$. Meanwhile we note that this choice of threshold is applicable to our present flow configuration, whereas for its extension to others caution should be taken. This choice of threshold value, on the other hand, is indispensable for making δ collapse onto δ_{99} on the upstream ZPG region, as illustrated in Fig. 6(a). Regarding the influence of the concave surface, we find that the boundary layer is considerably thinned, and the wall-shear stress exhibits notable increase (not shown here), consistent with previous studies.

From another angle, Prandtl's concept of boundary layer underlines the absence of viscosity effect or eddy viscosity in the flow region passing overhead, and it then follows that the edge of the turbulent boundary layer can be defined as the height where the uppermost turbulent motions can reach. Keeping this inspiration in mind, we determine the boundary layer thickness by considering the intermittency function γ, which by definition renders the probability of turbulent fluids protruding a certain wall-normal height. The implementation contains two steps.

The first step is to distinguish the turbulent fluids from the inviscid flow or, equivalently, to identify the turbulent-nonturbulent interface (TNTI) [55] prevalent in the outer boundary layer. Among the available detecting approaches for TNTI [56], we herein adopt the vorticity magnitude criterion, i.e., $|\omega^+| \equiv (\omega_i^+ \omega_i^+)^{1/2}$, similar to other boundary layer studies [57,58]. The vorticity criterion has a clear physical basis in that vorticity fluctuations can be produced by turbulent motions but not inviscid mechanisms, and therefore the turbulent flow can be separated from the nonturbulent region by a vorticity isosurface of low-magnitude value (i.e., the threshold th_ω). For determining the threshold value, we consider the whole flow field and calculate the volume fraction of the fluids the vorticity magnitude of which is greater than a particular value. As shown in Fig. 6(b), the profile of volume fraction decreases with increasing $|\omega^+|$. Importantly, the volume fraction exhibits a particular shape: it creates an inflection point at the intermediate value region where the decreasing
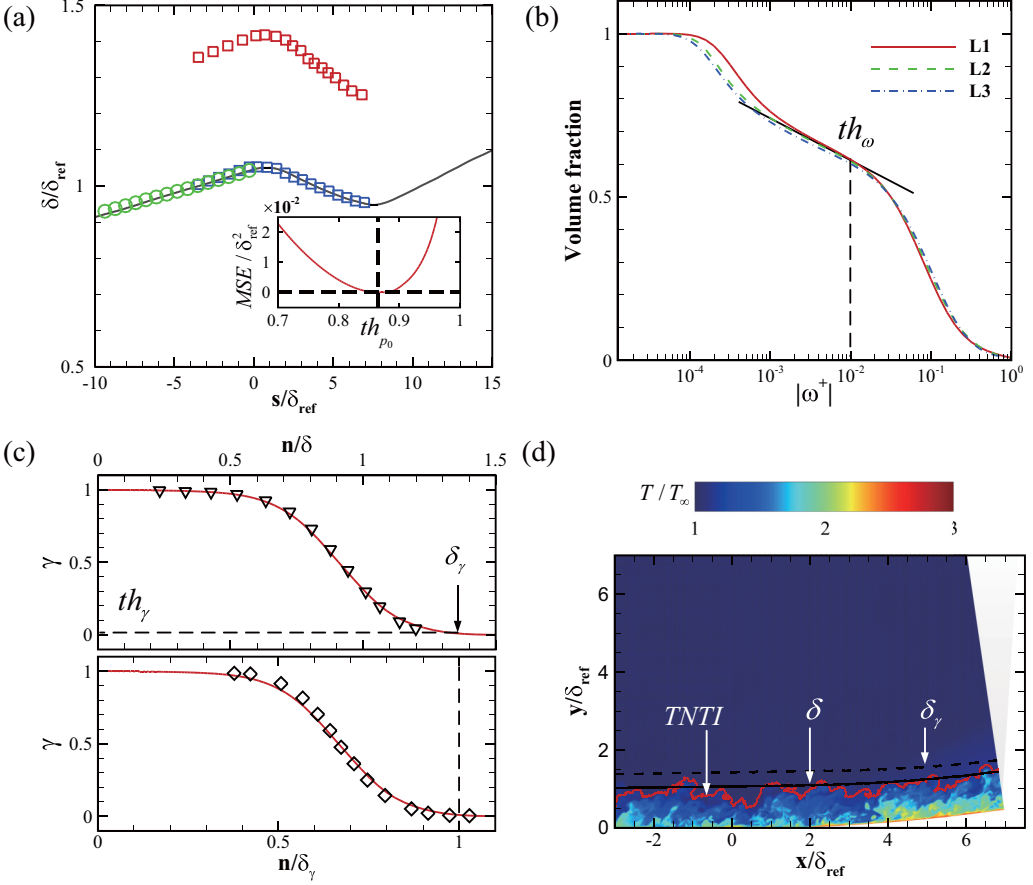
FIG. 6. (a) Boundary layer thickness δ (black line) for the whole domain, compared with δ_{99} (circles) for the upstream ZPG region. Red squares denote the thickness δ_γ measured from the γ profile by adopting the threshold $th_\gamma = 0.01$, and blue squares are wall-normal positions with $\gamma = 0.3$. The inset describes the thresholding $th_{p_0} \approx 0.86$ at the error minimum (marked by dashed lines). (b) Volume fraction of regions with vorticity magnitude larger than $|\omega^+|$. (c) Measurement of thickness δ_γ. Upside-down triangles are data from Borrell and Jiménez [60], and diamonds are from Chauhan *et al.* [61]. (d) A snapshot illustrating the boundary layer thicknesses.

rate slows down (sketched by a slope). In practice, any value around the inflection point can be taken as the threshold for TNTI detection [59]. Meanwhile it is worthwhile noting that three profiles collapse very well around the inflection point, suggesting that a uniform threshold can be adopted throughout the concave surface. As a consequence, the threshold is determined as $th_\omega = 0.01$ for the whole flow. The proper TNTI detection allows a binary representation of the flow field. The regions with $|\omega^+| > th_\omega$ are considered as turbulent and assigned a value of 1, and the rest are assigned a value of zero. The ensemble average of the binary representation directly gives the profile of intermittency function, as shown in the top plot of Fig. 6(c). The present intermittency function falls in very good agreement with the incompressibility data [60], meaning that the intermittency characteristics of two flow regimes remain similar, consistent with Morkovin's hypothesis [5]. As a side note, a large portion of turbulent fluids exceeds the commonly used δ_{99} or equivalently the present δ.

The second step measures the boundary layer thickness from the intermittency function, based on the idea of boundary layer edge constraining turbulent motions. For a meaningful measurement,
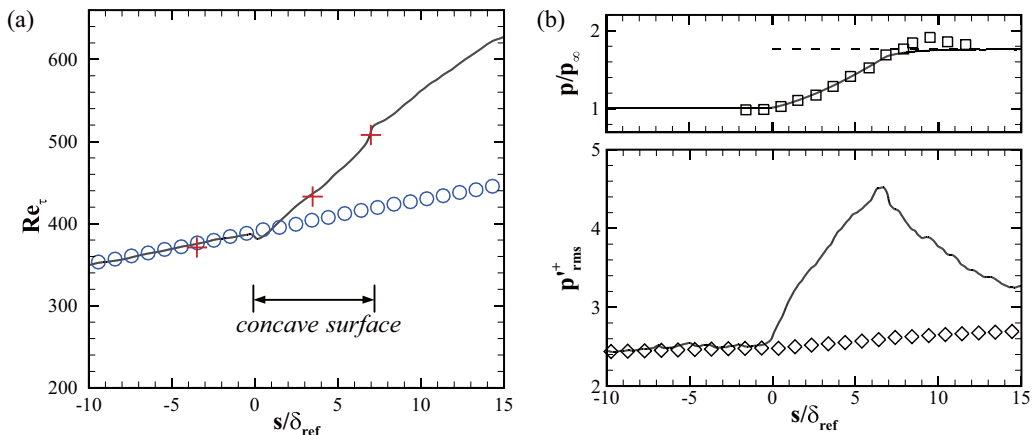
FIG. 7. (a) Evolution of Re_τ for the concave surface (line), compared with the canonical counterpart (circles). Crosses mark locations $L1$–$L3$. (b) Mean pressure p/p_∞ (solid line), in comparison with experimental data [17] (squares) and isentropic prediction (dashed line). RMS level $p_{rms}'^+$ (solid line), accompanied by the empirical prediction (diamonds) for the canonical turbulence.

we adopt a low-magnitude threshold (say th_γ) for the intermittency function, and the threshold value is determined by reference to available investigation [61]. To be more specific, the resulting boundary layer thickness (denoted by δ_γ for convenience) is equal to the intercept of the γ profile with the threshold value (i.e., $th_\gamma = 0.01$ in the present analysis) on the wall-normal axis n. The bottom plot of Fig. 6(c) utilizes δ_γ as the outer unit and compares the resulting γ profile with previous investigation [61], where the boundary layer thickness is determined by thresholding the probability distribution of TNTI.

Relying on this two-step procedure, the resulting boundary layer thickness is shown in Fig. 6(a) by red squares. We note that the thickness δ_γ follows the same trend with the thickness δ and is roughly 30% larger throughout the concave region. This means that two sets of thicknesses are physically consistent since they are simply connected by a fixed proportional factor. Furthermore, investigations have been conducted to figure out the connections between the intermittency and the thickness δ determined previously. We find that the wall-normal position with $\gamma = 0.3$ (blue squares) coincides very well with the boundary layer thickness δ. This demonstrates that the total pressure criterion leads to a uniform definition of boundary layer thickness, in the sense that the thickness δ possesses the uniform level of intermittency throughout the concave surface. As an aside, there exist other alternatives for defining the boundary layer thickness, such as the approach of utilizing the pseudovelocity (calculated through the integral of vorticity) [62]. Figure 6(d) shows two sets of boundary layer thicknesses in one snapshot, where the detected TNTI is overlaid on the contour of instantaneous temperature. This visualization conveys that the turbulent motions frequently protrude beyond the thickness δ but are well bounded by thickness δ_γ. We also note that the boundary layer thickness δ can work as a reasonable analogy of δ_{99} and is adopted in the following analysis to ease comparisons with other studies.

A useful quantity in characterizing the development of turbulent boundary layer is the friction Reynolds number Re_τ, which, defined as the ratio of boundary layer thickness δ to viscous lengthscale δ_ν (i.e., $Re_\tau = \delta/\delta_\nu$), manifests the scale separation across the whole layer. Figure 7(a) shows Re_τ versus wall-parallel distance. The observation is that the scale separation between the inner and outer layers is enlarged throughout the concave surface, as evidenced by the rapid increase in Re_τ compared with the canonical counterpart. This additionally implies that viscous lengthscale decreases more severely than boundary layer thickness during the flow distortion.

The wall pressure can be conveniently used to exhibit the flow response. Figure 7(b) depicts the mean pressure and rms values versus the wall-parallel distance. As expected, the mean wall
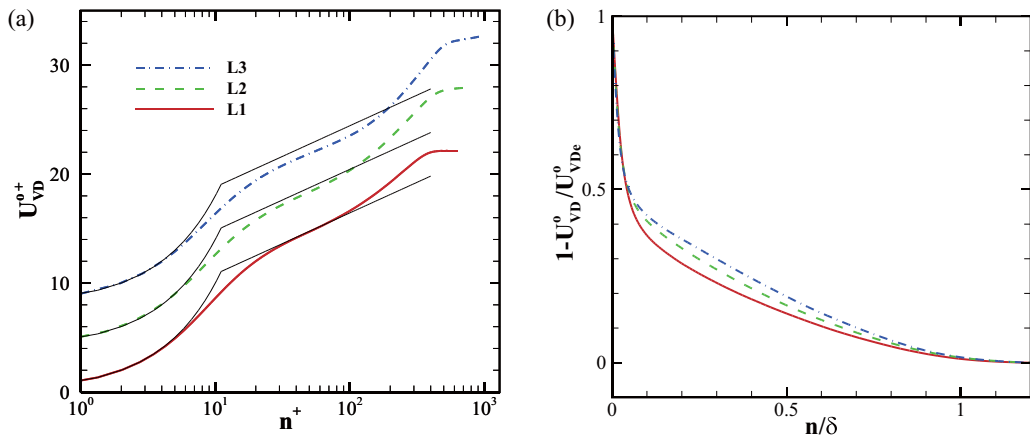
FIG. 8. (a) Profiles of the van Driest transformed velocity (thick lines) for locations $L1$–$L3$ from bottom to top (shifted by $U_{\mathrm{VD}}^{o+} = 4$). The incompressible law of the wall is shown by thin lines. (b) The mean defect velocities.

pressure is invariable on the upstream flat plate, it exhibits a rapid increase upon the concave wall, and it approaches the isentropic prediction downstream through a gradual variation. Good agreement is found with the experiment [17], being another validation. In addition, the inviscid flow is characterized by a decrease in Mach number from 2.87 to 2.50, a rise of density by a factor of 1.5, and a decrease in velocity by a factor of 0.95. The rms level p'_{rms} is compared with the predicted value utilizing the empirical correlation [63], which is established for the canonical flows and expressed as

$$p'^2_{\mathrm{rms}}/\tau_w^2 = 2.27 \log \mathrm{Re}_\tau - 7.36. \tag{3}$$

The agreement is very good on the upstream ZPG region. Notably, the p'_{rms} level exhibits considerable increment upon the concave surface, indicating that the pressure-carrying eddies passing overhead are energized. Downstream from the curved region, the p'_{rms} level drops towards the unperturbed level, demonstrating the boundary layer enters the stage of relaxation. Nevertheless, we note that the downstream flat plate (roughly $7\delta_{\mathrm{ref}}$ long) is insufficient to cover the full relaxation stage, and the related issues are left for further studies.

2. Velocity statistics and turbulence amplification

The streamwise mean velocity is first investigated for insights into the flow distortion. For meaningful comparisons, the velocity is projected onto the wall-normal coordinate n, and van Driest transformation is implemented to scale out the weak compressibility. Figure 8(a) highlights that the mean velocity well maintains the linear distribution in the viscous sublayer but deviates from the universal logarithmic distribution in the log region, with the appearance of a dip. This observation is consistent with the previous finding [17]. The formation of a dip is explained as that the turbulent lengthscales in this perturbed turbulence grow faster than in the unperturbed case [8], and this explanation is further aided by the present structural analysis shown in Sec. III B. Figure 8(b) depicts the mean defect velocities. It is noted that the velocity-defect law is violated in this distorted case, with the appearance of larger velocity deficit in the outer layer.

For an overall view of the turbulence evolution, Fig. 9 illustrates the absolute levels of streamwise turbulent intensity at various longitudinal stations, in company with the (high-Reynolds-number) experiment [17]. We note that these comparisons are meaningful since outer scales are employed for normalization, assuming that outer-scaled statistics are insensitive to Reynolds number (in the outer boundary layer). This assumption can be understood through a dimensional analysis of
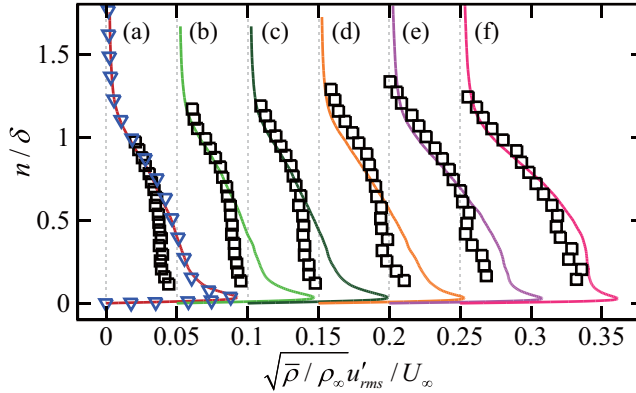
FIG. 9. The absolute levels of streamwise turbulent intensity (lines denote the present DNS), accompanied by the experimental data (squares) [17] at various longitudinal stations, which correspond to $s/\delta_{\mathrm{ref}} = -0.5$ (a), 0.5 (b), 1.0 (c), 3.0 (d), 5.0 (e), and 7.0 (f). Upside-down triangles denote DNS data at $M_\infty = 3$ and $\mathrm{Re}_\tau = 403$ [63], included to validate our simulation regarding the upstream ZPG TBL.

outer-layer statistics, and has been moreover examined by us through compilations of literature DNS datasets (e.g., Ref. [40]). Normally, one would expect this assumption to be more applicable for high Reynolds numbers wherein sufficient scale separation is present. As can be seen in Fig. 9, our DNS generally agrees with the experiment, and this agreement is fairly good in the outer region of TBL. By careful inspections, we note that discrepancies appear approaching the wall, but they are already emerged from the upstream ZPG TBL, where our data collapse excellently with one comparable DNS of ZPG TBL [63]. Basically, this implies that the existing discrepancies can be (partly) attributed to the disparity in Reynolds number: the outer-layer statistics of our simulation suffer certain low-Reynolds-number effect. Another important finding is that the inspected turbulent intensity exhibits considerable increase throughout the concave surface, which points towards the phenomenon of turbulence amplification.

The scaling of Reynolds stresses is examined at the streamwise locations $L1$–$L3$, as shown in Figs. 10(a) and 10(b). The Reynolds stresses mathematically correspond to the mean products of velocity fluctuations derived from Reynolds-stress transport equations, and they are herein computed in the Cartesian coordinates. As can be seen in Fig. 10(a), the profiles for the streamwise turbulent stress are different in shape, and the outer scaling does not succeed in collapsing them (nor does the inner scaling). Notably, considerable increase is observed for the streamwise turbulent stress throughout the concave surface, even though the weak compressibility (i.e., mean density variations) has been compensated here. This observation conveys that the turbulent motions are highly energized throughout the concave surface. The evolution of Reynolds shear stress is included in Fig. 10(b), where a pronounced increase is indeed observed in the outer layer. We should note that the reduction and even negative value observed for shear stress ($-R_{12}^+ < 0$ near the wall) are not contradictions to the turbulence amplification. Rather, those are caused by the mathematical contaminations between longitudinal and wall-normal velocities in Cartesian coordinates, since the influence of flow turning is not offset therein, as explained in the following.

For insights into the stress-bearing eddies, we conduct the quadrant analysis [64], which exploits the joint probability density function of velocity fluctuations in the $u - v$ plane, as sketched in Fig. 10(c). We also note that the orthogonal coordinates are considered for investigating the character of stress-bearing eddies, because in that way the artifacts induced by flow turning can be eliminated. From a mathematical standpoint, quadrant analysis conveys that the velocity fluctuations in wall turbulence have a dominant distribution in the second quadrant (ejection event) and fourth quadrant (sweep event), which produce positive contribution to the total mean product, namely, the shear stress. Particularly, the quadrant analysis has a close connection with the physical model of
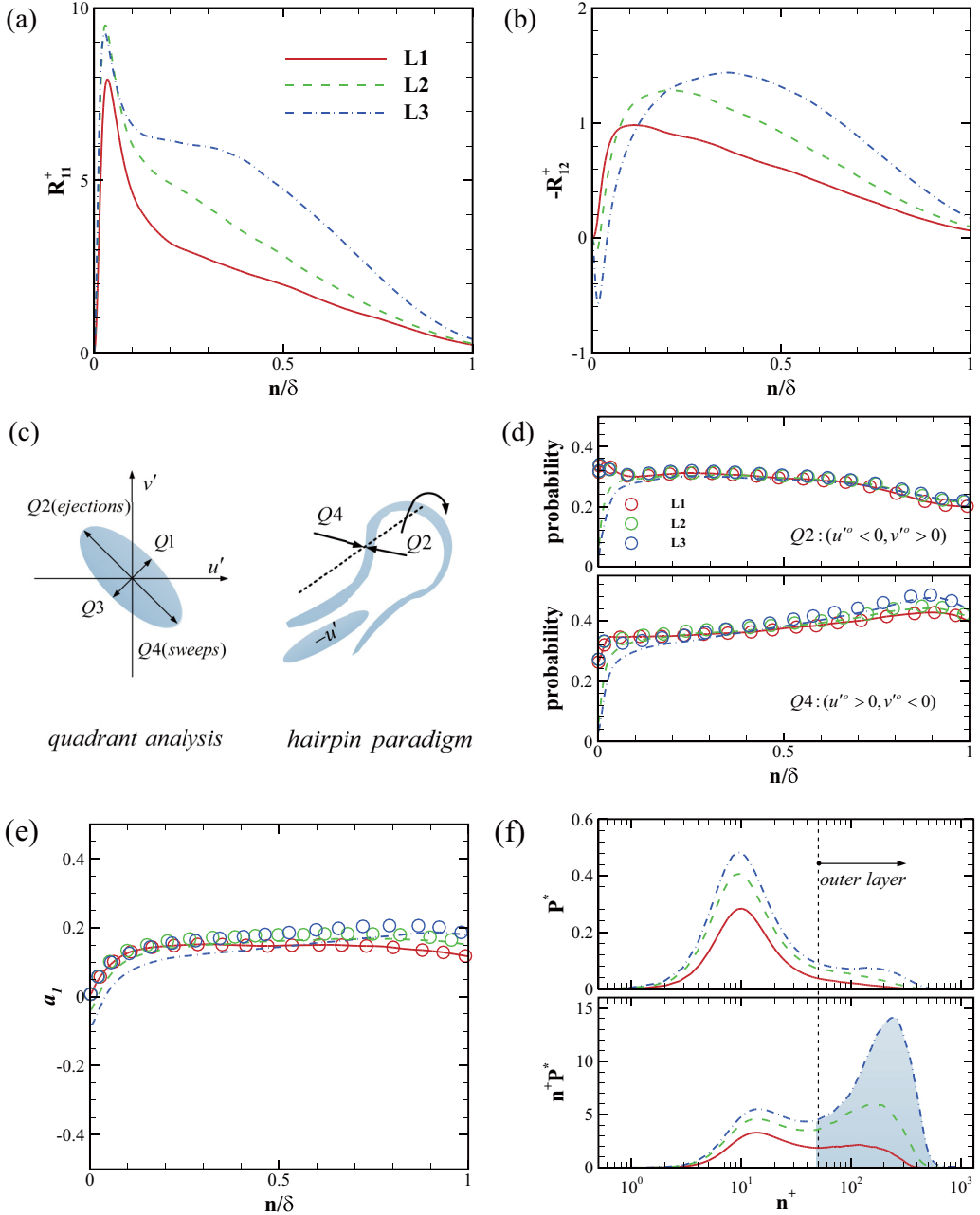
FIG. 10. Distributions of density-scaled Reynolds normal stress R_{11}^+ (a) and shear stress $-R_{12}^+$ (b), shown by colored lines. Reynolds stresses are denoted by $R_{ij}^+ = (\bar{\rho}/\bar{\rho}_w)\overline{u_i' u_j'}/u_\tau^2$. (c) Quadrant analysis and hairpin paradigm. (d) Probability of ejections and sweeps. (e) Structure parameter. In (d) and (e), colored circles denote results calculated in the orthogonal coordinates for locations $L1$–$L3$ respectively, and colored lines are results in Cartesian coordinates. (f) The distributions of turbulence production P^* (top) and its premultiplied counterpart $n^+ P^*$ (bottom) in the local inner coordinate for three streamwise locations L1–L3. The asterisk means normalization by reference wall units to exhibit absolute level. The shaded area denotes the outer-layer contribution.

the hairpin [65] in the sense of accounting for shear stress production. The ejections and sweeps can be regarded as the outward and inward inrush flows caused by the hairpin vortex, and the creation of shear stress corresponds to the net transport of axial momentum in the transverse direction (i.e., the direction normal to the mean streamline). With this aspect, we note that the coordinate s roughly matches the mean streamlines [see Fig. 3(a)], and thus the influence of flow turning can be offset when investigating the velocity fluctuations in the orthogonal coordinates system.

Figure 10(d) shows the probability of ejection and sweep events (colored symbols) for the selected locations $L1$–$L3$. Results obtained in the Cartesian coordinates system (colored lines) are still included for comparisons. It is surprising to find that the occurrences of ejections and sweeps are (essentially) unaffected by the concave surface, demonstrating that the stress-bearing eddies have not changed in character. This implies that the amplification of Reynolds stresses can be attributed to the alteration of the hairpin vortex in number or strength. This opinion agrees with the conjecture by Bradshaw [66] that the large scales can be considered as universal in shape, changing only by velocity and lengthscale factors. As an aside, the velocity fluctuations obtained in Cartesian coordinates (colored lines) lose the dominant distributions in second and fourth quadrants near the wall, which explains the appearance of negative shear stress therein. Illustrated in Fig. 10(e) is the structure parameter $a_1 = -\overline{u'v'}/\overline{u'_i u'_i}$. Indeed, the structure parameter displays rather less variation than the Reynolds stresses themselves, which also supports the perspective of stress-bearing eddies being unchanged, at least for the concave surface specified here. This finding would be valuable for modeling turbulence dynamics since it conveys that the coherent motions remain unchanged in organizing the distributions of Reynolds stresses even in the distorted case.

So far, the mechanism of turbulence amplification remains less clear, and insights are herein gained by inspecting the production term of turbulent kinetic energy, which is expressed as $P = -\overline{\rho u''_i u''_j} \partial \tilde{u}_i / \partial x_j$. To figure out the amplification, we illustrate the turbulence production by its absolute level and adopt the reference wall units for its normalization. The top plot of Fig. 10(f) depicts the production term in its local inner coordinate (n^+) for three streamwise locations $L1$–$L3$. It is highlighted that turbulence production locally attains the highest level in the near-wall region, and this peak is well situated within the thin buffer layer (roughly at $n^+ \approx 12$), even under flow distortion. This semilogarithmic plotting, as frequently adopted in literature, however, provides few visual impressions regarding the local contribution (i.e., the product Pdn^+) of turbulence production at a particular wall-normal position. For a graphical representation of the relatively local importance, premultiplied plotting is herein employed, as shown at the bottom of Fig. 10(f). To be more specific, equal area under each curve profile indicates equal integral contribution to the total turbulence production. This point is clear considering the mathematical equivalence between Pdn^+ and $n^+ Pd(\log n^+)$. As can be seen, the most difference between two plots lies in the outer layer: the premultiplied plotting unveils the increasingly pronounced contribution of the outer layer (shaded region), which is otherwise masked by the original plotting. For a quantitative assessment of outer-layer importance, we calculate the proportion of the shaded area to the total area under each curve profile. Again, the bounds of the outer layer are adopted following Pope [47]. This proportion turns out to be 37, 53, and 67% for streamwise locations $L1$–$L3$, respectively. It is to be expected that for a low-Reynolds-number ZPG turbulent boundary layer (i.e., at the reference location) the turbulence production is dominated by the near-wall region. This situation, however, has changed in the distorted case. Our analysis convincingly demonstrates that throughout the concave surface the outer layer holds an increasingly important role in turbulence production and can even override the near-wall region to become the dominant contributor.

For a global picture of the turbulence amplification, Fig. 11(a) illustrates the turbulent kinetic energy (i.e., $k = 1/2\overline{u''_i u''_i}$) throughout the entire concave surface, normalized by local wall units. It is highlighted that the turbulent boundary layer is continuously energized as passing the concave surface, and this trend is eye-catching in the outer layer. This makes sense because the destabilizing effect of the concave surface accumulates and larger perturbation leads to larger turbulence amplification. To understand the response process, we calculate the amplification ratio of turbulent
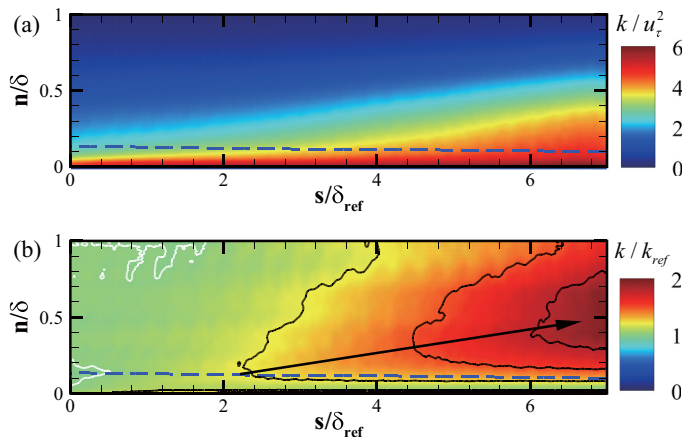
FIG. 11. (a) Contour of turbulent kinetic energy k normalized by local wall units throughout the entire concave surface. (b) Contour of amplification ratio k/k_{ref}. Contour lines (solid black) are shown at levels of 1.2, 1.5, and 1.8. White lines enclose the minor regions with $k/k_{ref} < 1$. In (a) and (b), the dashed line marks the lower bound of the outer layer.

kinetic energy for each wall-normal position in the local outer coordinate n/δ, and Fig. 11(b) shows the contour of k/k_{ref} as the function of wall-parallel distance and wall-normal height. Two observations can be made. First, the outer layer (bounded by the dashed line) experiences larger amplification than the near-wall region. This finding is in line with the above notion that the turbulence production is more pronounced in the outer layer. Second, the amplification ratio is not uniform across the wall-normal direction, and the amplification process is initiated by a peak value close to the wall, the wall-normal position of which departs outwards as the flow passes downstream (sketched by arrow). This observation supports the scenario whereby the response of the boundary layer propagates outwards from the wall. Furthermore, this process can be traced to the same mechanism found in wall-bounded turbulence that the outer layer is relatively slow in fading the upstream or history effects [39].

Until now, it is still unclear what kind of turbulent structures is responsible for the observed turbulence amplification. We herein investigate the premultiplied spanwise spectra of streamwise velocity fluctuations, with the aim of figuring out energy distributions versus different wavelengths. We take the reference TBL as an example for basic descriptions [see Fig. 12(a)]. As can be seen, an energy peak appears in the thin buffer layer and is characterized by a spanwise wavelength of $\lambda_z^+ \approx 100$. This dominant peak, commonly denoted as the "inner site," corresponds to the energetic signature of elongated low- and high-speed streaks [67]. It is worthwhile noting that recent studies towards high Reynolds numbers unveil another energy peak residing in the log region (i.e., the "outer site"), which represents the very long meandering features of low-momentum fluids flanked by high-momentum regions [28]. However, the outer site is not present here due to the current low Reynolds number. By examining Figs. 12(b) and 12(c), two observations can be made regarding the influence of the concave surface. First, the large-scale structures are energized in the outer layer, and even lead to a new energetic peak situated in the lower wake region ($n/\delta \approx 0.4$), which coincide with the wall-normal position of peak turbulence amplification. This suggests close connections between outer-layer large-scale structures and turbulence amplification. Second, the near-wall region, although still dominated by near-wall streaks, exhibits convincing evidence of large-scale energy overlaid by outer-layer structures. This observation points to enhanced interactions between the inner and outer layers, as will be elaborated in Sec. III C.
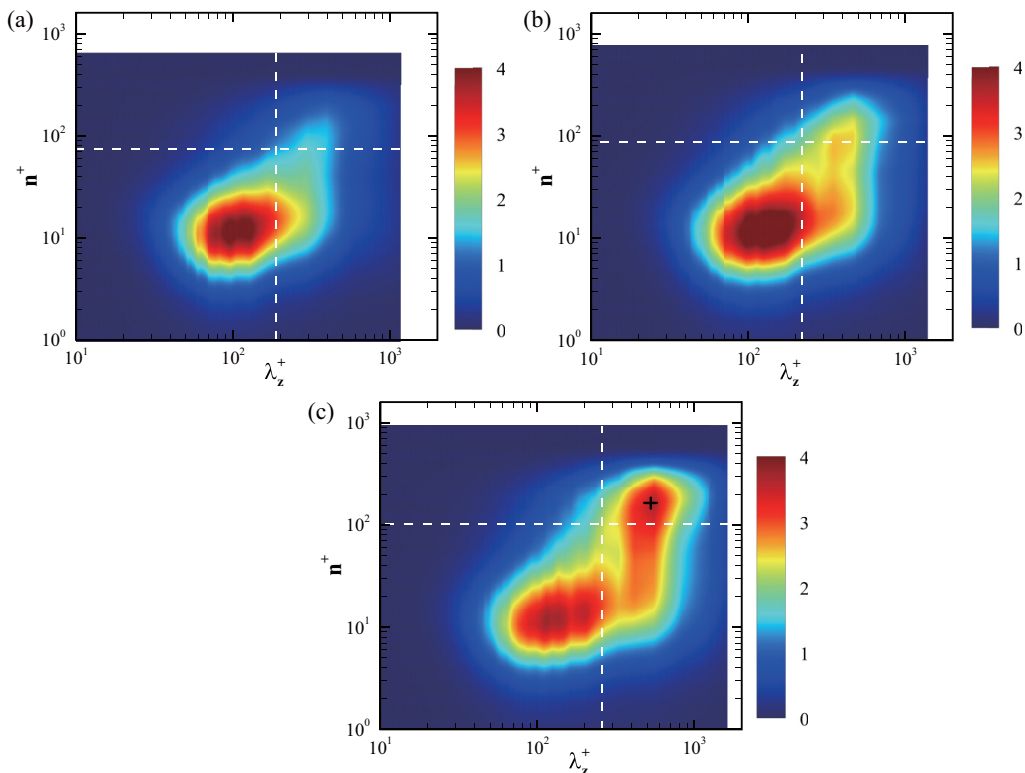
FIG. 12. Premultiplied energy spectra of streamwise velocity fluctuations $\bar{\rho}/\bar{\rho}_w k_z \Phi_{uu}^+$. The vertical dashed line marks the wavelength of 0.5δ, and the horizontal one shows the upper bound of the log region ($n/\delta = 0.2$) for each streamwise location. (a)–(c) correspond to locations $L1$–$L3$, respectively. The cross in (c) denotes the energy peak located in the lower wake region.

B. Flow organization

Keeping in mind the close relationship between statistics and structures, we herein investigate the responses of typical organized motions populating the turbulent boundary layer. Specifically, the streaky motions residing in the buffer and log layer are studied in the wall-parallel planes, which correspond to the wall-normal positions of $n^+ = 12$ and $n/\delta = 0.15$, respectively. This analysis combines spanwise two-point correlation with instantaneous visualizations to figure out the structural modification.

1. Near-wall streaks

The fluctuations of streamwise velocity (shown in Fig. 13) highlight the typical alternating streaky pattern in the near-wall region, with the low- and high-speed streaks rendered by dark and white speckles, respectively. These streaks, along with the accompanying quasistreamwise vortices, constitute the well-known near-wall cycle [25], which is responsible for turbulence sustaining. We note that the dynamics of near-wall streaks remain essentially unchanged throughout the concave surface: they meander significantly in the spanwise direction and branch in some instances when advected downstream. By careful inspections, we notice that near-wall streaks become progressively smaller in terms of their physical dimensions, and meanwhile there appears striking emergence of large-scale organization, which is comparable to the dimension of boundary layer thickness. These opposite trends in physical dimensions visually support the enlargement of scale separation
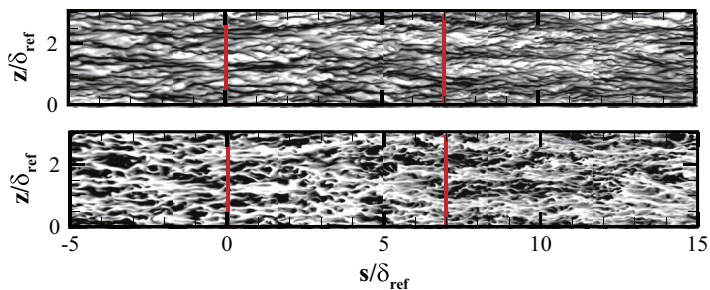
FIG. 13. Instantaneous fluctuations for streamwise velocity (top) and temperature (bottom) in a wall-parallel plane located at $n^+ = 12$. Contour levels are shown for $-0.2 \leqslant u'/u_\infty \leqslant 0.2$ and $-0.2 \leqslant T'/T_\infty \leqslant 0.2$, from dark to light shades.

throughout the concave surface. It is worth noting that the large-scale patterns, being present in the buffer layer, exhibit remarkable similarity with the log-region events (see Fig. 15). This means that they are actually the footprint of outer-layer motions passing overhead, consistent with the large-scale energy superimposition in energy spectra. Importantly, we observe that over the concave surface the near-wall streaks tend to be clustered as packages, and groups of streaks can be found residing within the positive or negative large-scale footprint. This visual impression points to the strengthening of inner-outer interactions, and will be quantitatively assessed in Sec. III C. An examination of the temperature field shows the similar streaky patterns but with the fluctuations (roughly) oppositely signed against the streaky patterns of u, providing a picture whereby outward ejections transport the low-speed and high-temperature fluids towards the upper layers.

For statistical evidences, two-point correlations of streamwise velocity fluctuations are used to characterize the spanwise dimension of turbulent structures, as shown in Fig. 14(a). The correlation function exhibits the typical positive-negative pattern, which reflects the alternating distribution of low- and high-speed streaks. Taking the reference TBL for basic descriptions, the correlation drops rapidly from the unit, and it attains the (first) minimum at a spanwise separation of $2\Delta z^+ \approx 100$, which corresponds to the average spacing of adjacent streaks. Regarding the influence of the concave surface, we observe that the first minimum moves to higher values
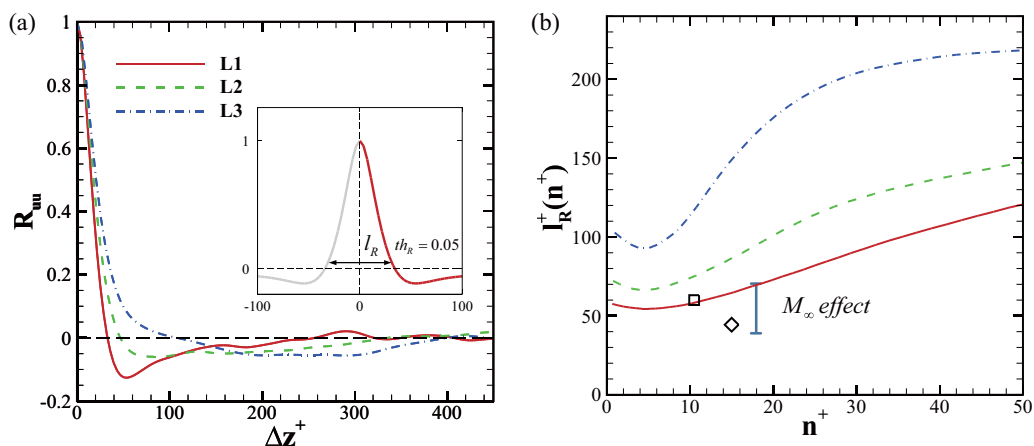

FIG. 14. (a) Spanwise two-point correlations of streamwise velocity fluctuations for streamwise locations $L1$–$L3$. (b) Distributions of characteristic lengthscales in the local inner coordinate, the measurement of which is sketched in the inset of (a). The Mach number effect covers the variations from the incompressible flow regime (square) [50] to a very high compressible regime (diamond) [4] at $M_\infty = 20$.
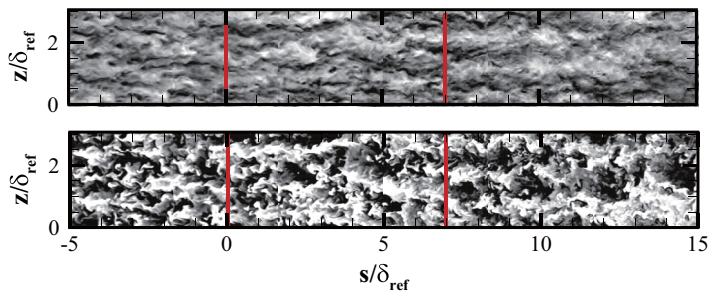
FIG. 15. Same as in Fig. 13 but extracted at wall-normal position $n/\delta = 0.15$.

(it even disappears), and a second flat minimum appears at larger spanwise separations. This demonstrates that there exists a wider modulation onto the small-scale streaky structures, in line with the visualizations. Another observation is that the crest portion of the correlation function (i.e., at small Δz^+) is widened, indicating that the widths or characteristic lengthscales of individual streaks have increased throughout the concave surface. For quantitative assessment, we determine the characteristic lengthscales following Hutchins *et al.* [68]. To be specific, at each wall-normal position we calculate the intercept of R_{uu} with a nominal threshold (i.e., $\mathrm{th}_R = 0.05$) on the positive axis, and the characteristic lengthscales of near-wall streaks are given by double the intercept, as sketched in the inset. Displayed in Fig. 14(b) is the resulting characteristic lengthscale, as the function of the wall-normal position in the inner coordinate. With little doubt, it can be said the characteristic lengthscales of turbulent structures have generally increased throughout the concave surface, suggesting the violation of the scaling for the near-wall region under turbulence distortion. Particularly, the characteristic lengthscales rise along with the wall-normal position, and this rising trend becomes more severe on the concave region than the unperturbed region, consistent with the previous notion [8].

We note that a convergence study has indeed been conducted regarding the correlation analyses (not detailed here), and it turns out that the reported data are sufficiently converged (although the correlations are not extremely smooth), which guarantees our conclusions are drawn with sufficient credibility. This convergence is probably to be expected because our sampling time period ($\Delta \mathrm{T}_s \approx 15\delta_{\mathrm{ref}}/u_\tau$), comparable to the well-accepted DNS (e.g., Ref. [38]), is long enough to make the correlations converged. For instance, the convergence of the characteristic lengthscales shown in Fig. 14(b) has been examined by considering another compilation, which covers a sampling time period of $\Delta T_s/2$, and it turns out that the maximum MSE between the two compilations is $\mathrm{MSE}/l_R^2(0) \approx 3 \times 10^{-3}$, meaning that the existing numerical uncertainty is far from severe enough to contaminate the physics. One might still be curious whether this change in lengthscale growth [shown in Fig. 14(b)] is the byproduct of Mach number variations during the inviscid turning (the present Mach number decreases from 2.87 to 2.50). However, it turns out to be not the case. We have included available literature data (symbols) covering from $M_\infty = 0$ to 20, and the Mach number effect is actually outside the modifications incurred by the concave surface.

2. Superstructures

An overview of the log-region structures is illustrated in Fig. 15 by fluctuations of streamwise velocity and temperature. In this plot, very long meandering regions of alternating negative and positive u fluctuations are clearly visible, which are termed superstructures in boundary layers [28]. This set of motions, maintaining a streamwise dimension of exceeding 6δ, is the outer-scaled dominant structures in the log region, in contrast to the large-scale motions (LSMs), which are characterized by the streamwise coherence of $2 - 3\delta$ [69]. It is also worth mentioning that superstructures are confined to the logarithmic region of boundary layers, contrasting with the far
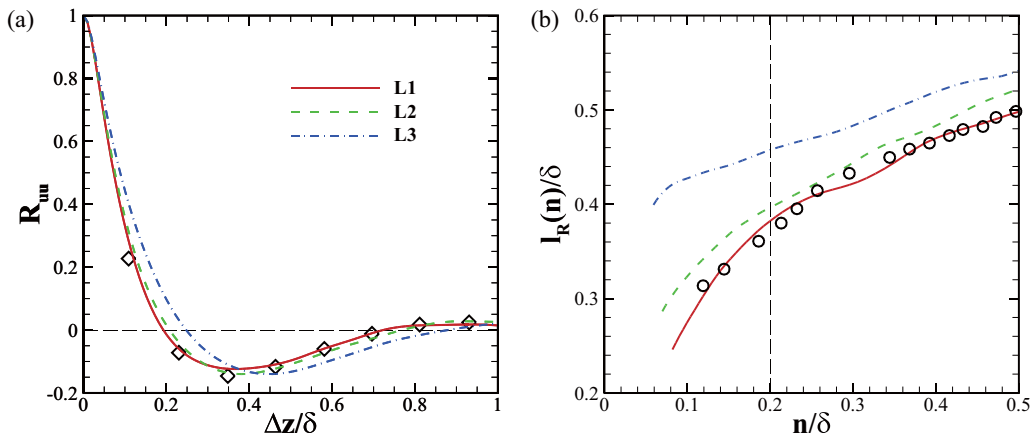
FIG. 16. (a) Spanwise two-point correlations of u fluctuations at $n/\delta = 0.15$. Diamonds denote incompressible data [28] at $Re_\tau = 1120$. (b) The characteristic spanwise lengthscales for log and lower-wake regions. The vertical dashed line marks the upper bound of the log region. Circles are data by Hutchins *et al.* [68].

extent of very large-scale motions in internal flows [27], and confusion should not be made between these two motions considering the structural differences [70]. From a three-dimensional view, the superstructures are forward-leaning with a mean inclination angle of $14°$ [71], accompanied by a pair of counter-rotating roll modes [30]. Particularly, they bring about complex inner-outer interactions by imposing a footprint onto the near-wall region. From the visualization, we note that these δ-scaled superstructures are modified by the concave surface: their streamwise and spanwise dimensions have increased. An examination of the temperature field demonstrates that the anticorrelation between streamwise velocity and temperature fluctuations is well maintained at this height.

Figure 16(a) illustrates the spanwise two-point correlations. Again, the incompressible (ZPG) data are included for comparison. We observe that the correlation function of the reference TBL agrees well with the experiment, consistent with the notions that compressibility remains weak at moderate Mach number [44] and superstructures are outer-scaled (i.e., insensitive to Reynolds numbers) [28]. Notably, a continuous increasing trend is observed for the spanwise length of superstructures, as evidenced by the widening of correlation functions throughout the concave surface. For an overall impression, Fig. 16(b) displays the characteristic lengthscales as determined previously but in local outer coordinates. As expected, considerable increases are observed for the characteristic lengthscales of log-region superstructures as well as for outer-layer LSMs. This observation demonstrates that the scaling of outer-layer turbulent structures (well established in canonical wall turbulence) is violated in the distorted case.

C. Turbulence modulation

The near-wall region, which had been believed to follow a purely viscous scaling in canonical turbulence, is by recent studies revealed to experience intense inner-outer interactions, since they live underneath the environment of large-scale energies from the outer layer. The modern perspective points out that these interactions comprise not only a purely linear superimposition of energy but also a subtle nonlinear effect termed amplitude modulation [29,72]. The linear superimposition is visible from the energy spectra, as shown in Sec. III A, while the nonlinear interaction is addressed in this section.

The amplitude modulation (AM) phenomenon was lately investigated by Hutchins and Marusic [73], where they found a high-degree coupling between the high- and low-pass-filtered components
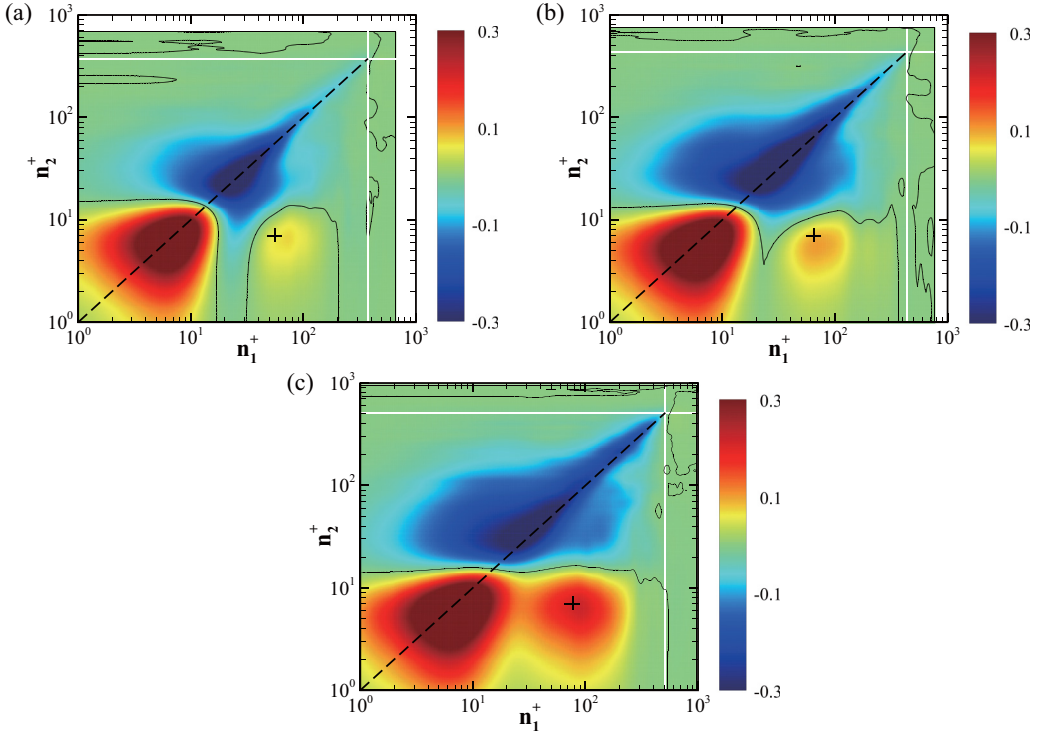
FIG. 17. Two-point AM covariance maps for the streamwise velocity component, with (a)–(c) corresponding to the streamwise locations $L1$–$L3$, respectively. White lines mark the boundary layer thickness δ, and black contour line marks a value of zero. Crosses mark the location $(0.15\mathrm{Re}_\tau, 7)$.

of near-wall fluctuations. A mathematical diagnostic tool was further developed by Mathis *et al.* [29] to quantify this relationship, which relies on a decoupling procedure by means of Hilbert transformation. Specifically, a spectral filter is first used to split the streamwise velocity fluctuations, of which the large-scale component (i.e., u'_L) acts as the modulating signal and the small-scale component (i.e., u'_S) is processed with the aid of Hilbert transformation to obtain the filtered envelope (i.e., u'_{EL}), and then a meaningful correlation coefficient R_u^{AM} (for u velocity) can be defined by correlating the large-scale fluctuations u'_L with the large-scale envelope u'_{EL} with the expression

$$R_u^{\mathrm{AM}} = \frac{\overline{u'_L u'_{EL}}}{\sqrt{\overline{u'^2_L}}\sqrt{\overline{u'^2_{EL}}}}. \tag{4}$$

This AM coefficient, at its very beginning, was proposed by Mathis *et al.* [29] to quantify the effect of amplitude modulation at two specific wall-normal points, which are separately located in the near-wall and log regions; nevertheless, it is argued that the implementation conducted at the same single point serves as a reasonable surrogate so that an overall view of AM effect can be provided across the whole layer. The latter attitude, however, had been critiqued by Schlatter and Örlü [74], who have mainly uncovered the close dependence of modulation coefficient on the data's skewness in mathematics. This difficulty was later on reconciled by Mathis *et al.* [75], who had shown that the modulation effect is actually embodied by one component of the skewness factor after scale decomposition and thus the mathematical dependence does not exclude physical meanings. These debates had pushed the AM coefficient towards a genuine two-point AM analysis. Bernardini and Pirozzoli [76] proposed a refined measure by traversing all the wall-normal positions, and
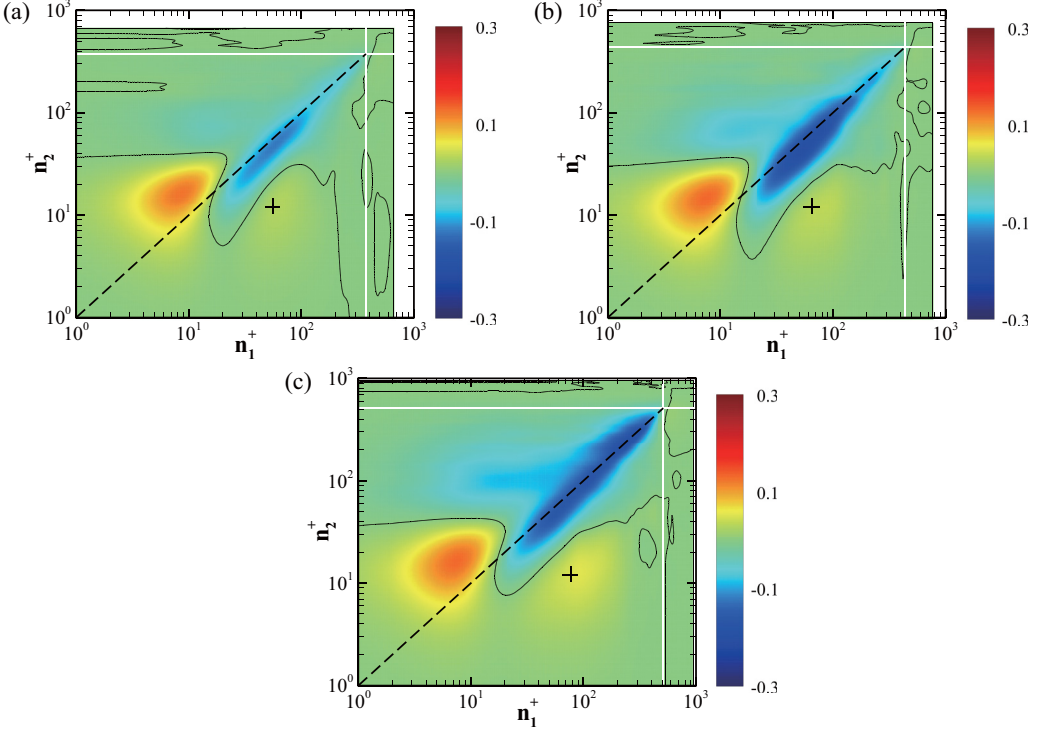
FIG. 18. Same as in Fig. 17, but with AM covariance for v velocity and crosses marking the location $(0.15\mathrm{Re}_\tau, 12)$.

utilized the AM covariance $C_u^{\mathrm{AM}}(y_1, y_2) = \overline{u_L'^+(y_1)u_{EL}'^+(y_2)}$ (for u velocity) to quantify the absolute modulation effect of large structures located at wall-normal position y_1 on small structures at y_2. The AM covariance provides a genuine representation of the top-down interaction, and is here adopted for the following analysis.

The AM covariance maps computed through a probe pair (i.e., wall-normal positions n_1 and n_2) are reported in Figs. 17–19 for the streamwise, wall-normal, and spanwise velocities, respectively. As a side note, no shifting in the streamwise direction has been made for the probe pair, since no quantitative difference can be caused by the inclination of coherent structures [76], and the extension of AM covariance to the transverse velocity components is simply by replacing the filtered envelope $u_{EL}'^+$ with the transverse counterparts. Following Bernardini and Pirozzoli [76], we have utilized a spectral filter (with the cutoff wavelength being $\lambda_z = 0.5\delta$, as sketched in Fig. 12) to split the velocities into large and small components in the spanwise direction. In addition, the Cartesian velocities are projected onto the orthogonal coordinates in order to avoid possible contamination between u and v velocity components, and the superscript "o" has been omitted in the following just for convenience.

We start our discussions with respect to u velocity, as depicted in Fig. 17. All the covariance maps show the typical two-peak pattern: a diagonal and off-diagonal peak. The former is mainly due to the high fluctuation intensity of u_s' near the wall, while the latter is linked with the genuine influence of the top-down nonlinear interaction. It is to be expected that positive values are observed in the near-wall region, providing a scenario in which the small-scale energy is enhanced by positive large-scale signals and depressed by the negative ones. In other words, the amplitude modulation is quantified by how much the positive large-scale events from the log layer override the negative ones in creating small-scale energy in the near-wall region. We also note that although
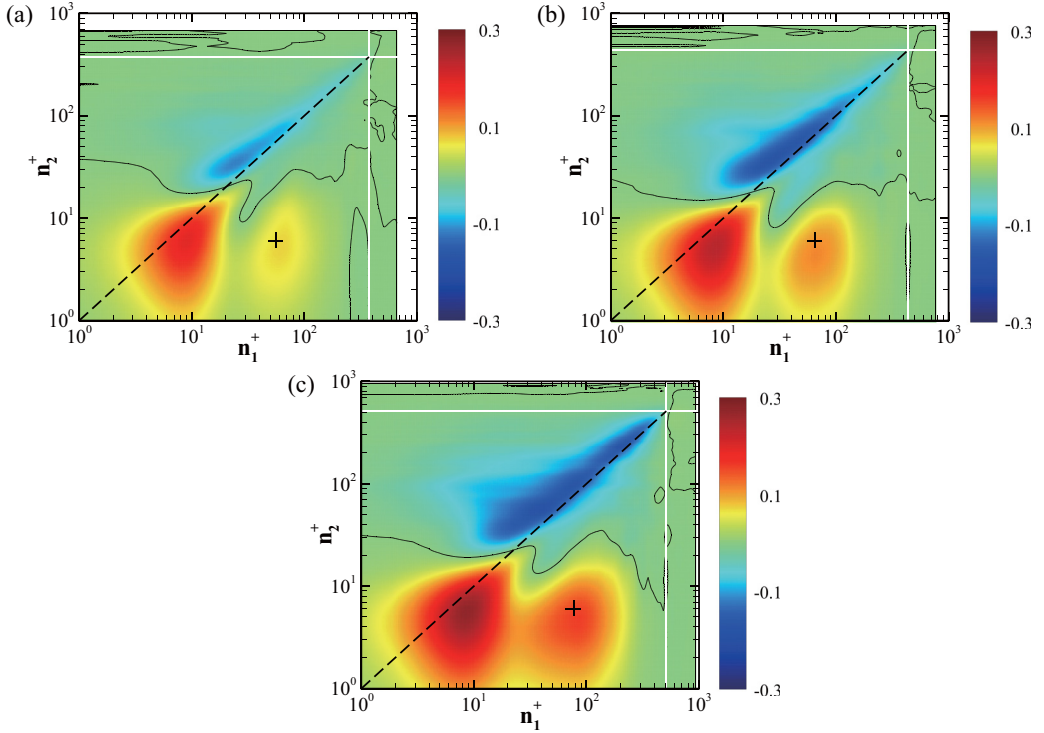
FIG. 19. Same as in Fig. 17, but with AM covariance for w velocity and crosses marking $(0.15\mathrm{Re}_\tau, 6)$.

the covariance map is roughly symmetric with respect to the diagonal line at the reference location $L1$ the contour is intensely distorted under the influence of the concave surface, forming a strongly amplified off-diagonal peak. By closer inspection, we find that the off-diagonal peak roughly occurs at the positions $n_1^+ = 0.15\mathrm{Re}_\tau$ and $n_2^+ = 7$ for all streamwise locations. This demonstrates that the amplitude modulation invariantly takes place between the log-region superstructures and the near-wall streaks over the concave surface, despite the energetic presence of LSMs in the lower wake region (see Fig. 12). Importantly, we find an increasing trend for the off-diagonal peak throughout the concave surface, which indicates enhancement to the inner-outer interactions, consistent with the flow visualizations. Regarding the AM covariance for transverse velocities shown in Figs. 18 and 19, we find that all the covariance maps exhibit similarities to the streamwise counterpart: they display the two-peak pattern with the modulating and modulated signal situated in the log region and buffer layer, respectively, and the concave surface highly increases the off-diagonal peak value, manifesting enhanced top-down modulation effect.

An overall picture provided by the phenomenon of amplitude modulation is one in which the near-wall energy is intensified under the high-speed large-scale events, due to the creation of a high local velocity gradient, and the opposite is true for the low-speed events [73]. To put it another way, the large-scale signature can penetrate onto the wall and produces local variations of wall-shear stress, which in turn serves as the input of small-scale energy in the near-wall region. It is currently known that the amplitude modulation holds a Reynolds number dependence [76]. In this sense, one could think of intense inner-outer interactions when scale separation is guaranteed by a sufficiently high Reynolds number. Keeping this in mind, it would be intriguing to figure out whether the present enhancement of modulation effect is merely a consequence of Reynolds number increasing during the flow distortion [see Fig. 7(a)] or due to the direct influence of the concave surface. In other words, the gain from Reynolds number effect should be separated for understanding the genuine contribution from the concave surface.
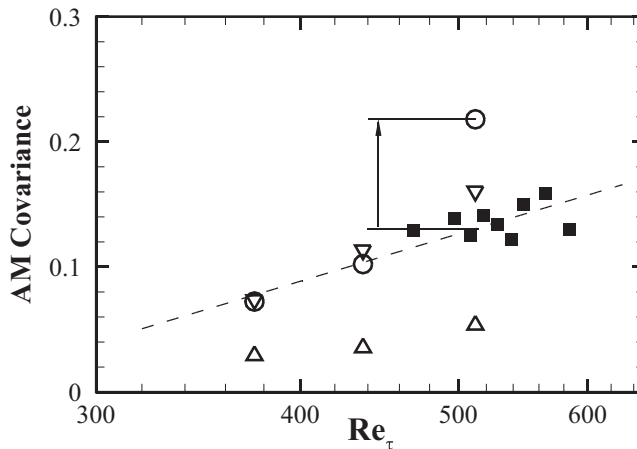
FIG. 20. Distributions of the off-diagonal peak in AM covariance for u (circles), v (triangles), and w (upside-down triangles) velocities. Squares denote DNS data for u [76], the fitted correlation of which, i.e., $0.17 \log(\mathrm{Re}_\tau) - 0.93$, is shown by the dashed line.

We report the off-diagonal peak values as a function of Re_τ in Fig. 20 for three velocities, along with the DNS data from the canonical case [76]. We start our discussions regarding the streamwise component. Very good agreement is first observed for the reference TBL with the empirical correlation (denoted by dashed line), which confirms the reliable implementation of the AM quantification procedure. Note that there is a generally logarithmic growth for the modulation effect versus friction Reynolds numbers [76]. Two observations can be made regarding the influences of the concave surface. First, we note that the AM strength conforms to the Reynolds-number-dependent trend very well up to the midpoint of the curved region, for the flow configuration specified here. This means that during the early stage of flow response the enhancement in modulation effect can be accounted for by the increase in friction Reynolds number. It is in this sense that the influence of the concave surface appears in an indirect manner. Second, a high magnitude well above the empirical prediction is observed at the end of the concave surface. This additional increment cannot be explained by the data scatter, and should be attributed to the genuine influence of the concave surface. This makes sense because the interacting components of the modulation process, i.e., the superstructures and near-wall streaks, are intensely modified by the concave surface, as evidenced by the growth in energy and characteristic lengthscales. As a consequence, the intensified superstructures create stronger footprints on the inner layer, and cluster more near-wall streaks together to form larger packets. Similar increasing trends are observed for the transverse velocities, although with different magnitudes. In addition, the AM effect magnitude for the wall-normal velocity is noticeably lower than the others, which is likely due to the blocking effect of the impermeable wall condition.

IV. CONCLUDING REMARKS

We have used DNS to study the flow physics of a supersonic turbulent boundary layer ($M_\infty = 2.87$) in response to a short region of the concave surface. The inspected boundary layer stands for a class of curvature-driven engineering flows, which are collectively influenced by the effects of concave streamline curvature, bulk compression, and adverse pressure gradients (their separate contributions are left for future study).

Overall, the turbulent boundary layer is severely distorted. Two consistent approaches are first employed to reasonably define the boundary layer thickness: one relies on total pressure, and the other exploits the intermittency function. It is confirmed that the concave surface generally leads to boundary layer thinning and wall-shear stress increasing, as the reflection of rapid rises in density.

As revealed by wall pressure, the turbulence is continuously amplified throughout the concave surface, and then starts relaxation on the following flat plate. The present paper focuses on the former stage of turbulence amplification.

Investigations of velocity statistics reveal that the scaling well established in canonical wall turbulence is generally violated in this distorted case. The mean streamwise velocity features a dip below the logarithmic distribution, and exhibits a larger velocity deficit in the wake region. The Reynolds stresses exhibit considerable increase across the boundary layer, which points towards the phenomenon of turbulence amplification. By examining quadrant events and structure parameter, we find that the stress-bearing eddies have not changed in character, suggesting their changes in number or strength finally lead to the increase in Reynolds stresses. The source of turbulence amplification is understood by investigating the production of turbulent kinetic energy. We reveal that an increasingly large proportion of turbulence production is contributed by the outer boundary layer, which on its largest level could account for twice as much as the near-wall counterpart (for the present configuration). We further reveal that the striking amplification of outer-layer turbulence is linked with the energization of large-scale motions therein, as evidenced by the energy spectra.

Structural analysis reveals that the organized coherent motions, which are well scaled in canonical wall turbulence, are modified by the concave surface, and they exhibit a general increasing trend in terms of characteristic lengthscales. Notably, we observe that the log-region superstructures overlay stronger footprints on the near-wall streaks, suggesting enhanced inner-outer interactions. More insights are gained by assessing the nonlinear component of the interactions using a mathematical tool. It is confirmed that the amplitude modulation is still dominated by log-region superstructures, despite the energization of large-scale motions in the lower-wake region. Importantly, we find the concave surface causes considerable enhancement to the turbulence modulation. The present paper collectively points towards the perspective that the concave surface endows the outer-scaled motions with a more prominent role in the turbulence dynamics, which may have implications for flow control strategies (e.g., drag reduction) targeting the large-scale structures.

[1] T. Maeder, N. A. Adams, and L. Kleiser, Direct simulation of turbulent supersonic boundary layers by an extended temporal approach, J. Fluid Mech. **429**, 187 (2001).

[2] S. Pirozzoli, F. Grasso, and T. B. Gatski, Direct numerical simulation and analysis of a spatially evolving supersonic turbulent boundary layer at M = 2.25, Phys. Fluids **15**, 530 (2004).

[3] L. Duan, I. Beekman, and M.P. Martin, Direct numerical simulation of hypersonic turbulent boundary layers. Part 3. Effect of Mach number, J. Fluid Mech. **672**, 245 (2011).

[4] M. Lagha, J. Kim, J. D. Eldredge, and X. Zhong, A numerical study of compressible turbulent boundary layers, Phys. Fluids **23**, 015106 (2011).

[5] M. V. Morkovin, Effects of compressibility on turbulent flows, in *Mécanique de la Turbulence*, edited by A. Favre (CNRS, Paris, 1961), p. 367.

[6] E. F. Spina, A. J. Smits, and S. K. Robinson, The physics of supersonic turbulent boundary layer, Ann. Rev. Fluid Mech. **26**, 287 (1994).

[7] J. C. Gills and J. P. Johnston, Turbulent boundary-layer flow and structure on a convex wall and its redevelopment on a flat wall, J. Fluid Mech. **135**, 123 (1983).

[8] P. Bradshaw, Effects of streamline curvature on turbulent flow, AGARDograph 169 (1973).

[9] A. J. Smits and J.-P. Dussauge, *Turbulent Shear Layers in Supersonic Flow*, 2nd ed. (AIP, New York, 2006).

[10] E. M. Fernando and A. J. Smits, A supersonic turbulent boundary layer in an adverse pressure gradient, J. Fluid Mech. **211**, 285 (1990).

[11] P. Bradshaw, The effect of mean compression or dilatation on the turbulence structure of supersonic boundary layers, J. Fluid Mech. **63**, 449 (1974).

[12] A. J. Smits and D. H. Wood, The response of turbulent boundary layers to sudden perturbations, Ann. Rev. Fluid Mech. **17**, 321 (1985).

[13] A. J. Smits, S. T. B. Young, and P. Bradshaw, The effect of short regions of high surface curvature on turbulent boundary layers, J. Fluid Mech. **94**, 209 (1979).

[14] A. J. Laderman, Adverse pressure gradient effects on supersonic boundary-layer turbulence, AIAA J. **18**, 1186 (1980).

[15] D. Degani and A. J. Smits, Effect of short regions of surface curvature on compressible turbulent boundary layers, AIAA J. **28**, 113 (1990).

[16] J. F. Donovan and A. J. Smits, A preliminary investigation of large-scale organized motions in a supersonic turbulent boundary layer on a curved surface, *19th AIAA, Fluid Dynamics, Plasma Dynamics, and Lasers Conference*, AIAA Paper No. 87-1285 (Princeton University, NJ, 1987).

[17] M. Jayaram, M.W. Taylor, and A. J. Smits, The response of a compressible turbulent boundary layer to short regions of concave surface curvature, J. Fluid Mech. **175**, 343 (1987).

[18] J. F. Donovan, E. F. Spina, and A. J. Smits, The structure of a supersonic turbulent boundary layer subjected to concave surface curvature, J. Fluid Mech. **259**, 1 (1994).

[19] D. R. Smith and A. J. Smits, A study of the effects of curvature and compression on the behavior of a supersonic turbulent boundary layer, Exp. Fluids **18**, 363 (1995).

[20] Q.-C. Wang, Z.-G. Wang, and Y.-X. Zhao, An experimental investigation of the supersonic turbulent boundary layer subjected to concave curvature, Phys. Fluids **28**, 096104 (2016).

[21] H. H. Fernholz and P. J. Finley, A critical commentary on mean flow data for two-dimensional compressible turbulent boundary layers, AGARDograph **253** (1980).

[22] J. Jiménez, Near-wall turbulence, Phys. Fluids **25**, 101302 (2013).

[23] S. K. Robinson, Coherent motions in turbulent boundary layers, Annu. Rev. Fluid Mech. **23**, 601 (1991).

[24] A. J. Smits, B. J. McKeon, and I. Marusic, High Reynolds number wall turbulence, Annu. Rev. Fluid Mech. **43**, 353 (2011).

[25] J. Jiménez and A. Pinelli, The autonomous cycle of near-wall turbulence, J. Fluid Mech. **389**, 335 (1999).

[26] W. Schoppa and F. Hussain, Coherent structure generation in near-wall turbulence, J. Fluid Mech. **453**, 57 (2002).

[27] K. Kim and R. Adrian, Very large-scale motion in the outer layer, Phys. Fluids **11**, 417 (1999).

[28] N. Hutchins and I. Marusic, Evidence of very long meandering features in the logarithmic region of turbulent boundary layers, J. Fluid Mech. **579**, 1 (2007).

[29] R. Mathis, N. Hutchins, and I. Marusic, Large-scale amplitude modulation of the small-scale structures in turbulent boundary layer, J. Fluid Mech. **628**, 311 (2009).

[30] K. M. Talluru, R. Baidya, N. Hutchins, and I. Marusic, Amplitude modulation of all three velocity components in turbulent boundary layers, J. Fluid Mech. **746**, R1 (2014).

[31] I. Marusic, R. Mathis, and N. Hutchins, High Reynolds number effects in wall turbulence, Int. J. Heat Fluid Flow **31**, 418 (2010).

[32] R. Mathis, I. Marusic, S. I. Chernyshenko, and N. Hutchins, Estimating wall-shear-stress fluctuations given an outer region input, J. Fluid Mech. **715**, 163 (2013).

[33] J. B. Anders, Outer-layer manipulators for turbulent drag reduction, in *Viscous Drag Reduction in Boundary Layers*, edited by D. M. Bushnell and J. N. Hefner, Progress in Astronautics and Aeronautics Vol. 123 (AIAA, Washington, DC, 1989).

[34] Y. Hwang, Near-wall turbulent fluctuations in the absence of wider outer motions, J. Fluid Mech. **723**, 264 (2013).

[35] X. L. Li, D.-X. Fu, and Y.-W. Ma, Direct numerical simulation of a spatially evolving supersonic turbulent boundary layer at Ma = 6, Chin. Phys. Lett. **23**, 1519 (2006).

[36] X.-L. Li, D.-X. Fu, Y.-W. Ma, and X. Liang, Direct numerical simulation of compressible turbulent flows, Acta Mech. Sin. **26**, 795 (2010).

[37] M. P. Martín, E. M. Taylor, M. Wu, and V. G. Weirs, A bandwidth-optimized WENO scheme for the effective direct numerical simulation of compressible turbulence, J. Comput. Phys. **220**, 270 (2006).

[38] J. A. Sillero, J. Jiménez, and R. D. Moser, One-point statistics for turbulent wall-bounded flows at Reynolds numbers up to $\delta^+ \approx 2000$, Phys. Fluids **25**, 105102 (2013).

[39] P. Schlatter and R. Örlü, Turbulent boundary layers at moderate Reynolds numbers: Inflow length and tripping effects, J. Fluid Mech. **710**, 5 (2012).

[40] P. Schlatter and R. Örlü, Assessment of direct numerical simulation data of turbulent boundary layers, J. Fluid Mech. **659**, 116 (2010).

[41] E. R. van Driest, The problem of aerodynamic heating, Aeronaut. Eng. Rev. **15**, 26 (1956).

[42] E. J. Hopkins and M. Inouye, An evaluation of theories for predicting turbulent skin friction and heat transfer on flat plates at supersonic and hypersonic Mach numbers, AIAA J. **9**, 993 (1971).

[43] A. J. Smits, N. Matheson, and P. N. Joubert, Low-Reynolds-number turbulent boundary layers in zero and favourable pressure gradients, J. Ship Res. **27**, 147 (1983).

[44] S. Pirozzoli and M. Bernardini, Turbulence in supersonic boundary layers at moderate Reynolds number, J. Fluid Mech. **688**, 120 (2011).

[45] P. Bookey, C. Wyckham, A. J. Smits, and M. P. Martín, New experimental data of STBL at DNS/LES accessible Reynolds numbers, AIAA Paper No. 2005-309 (2005), http://croccolab.umd.edu/publications/conf-docs/25-AIAA_2005_0309.pdf.

[46] S. Piponniau, J.-P. Dussauge, J. F. Devièbe, and P. Dupont, A simple model for low-frequency unsteadiness in shock-induced separation, J. Fluid Mech. **629**, 87 (2009).

[47] S. Pope, *Turbulent Flows* (Cambridge University, Cambridge, England, 2000).

[48] T. B. Nickels, I. Marusic, S. Hafez, N. Hutchins, and M. S. Chong, Some predictions of the attached eddy model for a high Reynolds number boundary layer, Phil. Trans. R. Soc. A **365**, 807 (2007).

[49] I. Marusic, J. P. Monty, M. Hultmark, and A. J. Smits, On the logarithmic region in wall turbulence, J. Fluid Mech. **716**, R3 (2013).

[50] J. Kim, P. Moin, and R. Moser, Turbulence statistics in fully developed channel flow at low Reynolds number, J. Fluid Mech. **177**, 133 (1987).

[51] M. Lagha, J. Kim, J. D. Eldredge, and X. Zhong, Near-wall dynamics of compressible boundary layers, Phys. Fluids **23**, 065109 (2011).

[52] M. Lagha, A comprehensible low-order model for wall turbulence dynamics, Phys. Fluids **26**, 085111 (2014).

[53] D. B. DeGraaff and J. K. Eaton, Reynolds number scaling of the flat-plate turbulent boundary layer, J. Fluid Mech. **422**, 319 (2000).

[54] J. A. Schetz and R. D. W. Bowersox, *Boundary Layer Analysis*, 2nd ed. (AIAA, Reston, Virginia, 2011).

[55] S. Corrsin and A. L. Kistler, Free-stream boundaries of turbulent flows, NACA Tech. Rep. TN-1244, Washington, DC (1955).

[56] C. B. da Silva, J. C. R. Hunt, I. Eames, and J. Westerweel, Interfacial layers between regions of different turbulence intensity, Annu. Rev. Fluid Mech. **46**, 567 (2014).

[57] J. Jiménez, S. Hoyas, M. P. Simens, and Y. Mizuno, Turbulent boundary layers and channels at moderate Reynolds numbers, J. Fluid Mech. **657**, 335 (2010).

[58] J. Lee, H. J. Sung, and T. A. Zaki, Signature of large-scale motions on turbulent/non-turbulent interface in boundary layers, J. Fluid Mech. **819**, 165 (2017).

[59] C. B. da Silva, R. R. Taveira, and G. Borrell, Characteristics of the turbulent/nonturbulent interface in boundary layers, jets and shear-free turbulence, J. Phys.: Conf. Series **506**, 012015 (2014).

[60] G. Borrell and J. Jiménez, Properties of the turbulent/non-turbulent interface in boundary layers, J. Fluid Mech. **801**, 554 (2016).

[61] K. Chauhan, J. Philip, C. M. de Silva, N. Hutchins, and I. Marusic, The turbulent/non-turbulent interface and entrainment in a boundary layer, J. Fluid Mech. **742**, 119 (2014).

[62] P. R. Spalart and M. K. Strelets, Mechanisms of transition and heat transfer in a separation bubble, J. Fluid Mech. **403**, 329 (2000).

[63] M. Bernardini and S. Pirozzoli, Wall pressure fluctuations beneath supersonic turbulent boundary layers, Phys. Fluids **23**, 085102 (2011).

[64] J. M. Wallace, Quadrant analysis in turbulence research: History and evolution, Annu. Rev. Fluid Mech. **48**, 131 (2016).

[65] R. J. Adrian, Hairpin vortex organization in wall turbulence, Phys. Fluids **19**, 041301 (2007).

[66] P. Bradshaw, The turbulence structure of equilibrium boundary layers, J. Fluid Mech. **29**, 625 (1967).

[67] S. J. Kline, W. C. Reynolds, F. A. Schraub, and P. W. Rundstadler, The structure of turbulent boundary layers, J. Fluid Mech. **30**, 741 (1967).

[68] N. Hutchins, W. T. Hambleton, and I. Marusic, Inclined cross-stream stereo particle image velocimetry measurements in turbulent boundary layers, J. Fluid Mech. **541**, 21 (2005).

[69] T. Saxton-Fox and B. J. McKeon, Coherent structures, uniform momentum zones and the streamwise energy spectrum in wall-bounded turbulent flows, J. Fluid Mech. **826**, R6 (2017).

[70] J. P. Monty, N. Hutchins, H. C. H. Ng, I. Marusic, and M. S. Chong, A comparison of turbulent pipe, channel and boundary layer flows, J. Fluid Mech. **632**, 431 (2009).

[71] I. Marusic and W. D. C. Heuer, Reynolds Number Invariance of the Structure Inclination Angle in Wall Turbulence, Phys. Rev. Lett. **99**, 114504 (2007).

[72] I. Marusic, W. J. Baars, and N. Hutchins, Scaling of the streamwise turbulence intensity in the context of inner-outer interactions in wall turbulence, Phys. Rev. Fluids **2**, 100502 (2017).

[73] N. Hutchins and I. Marusic, Large-scale influences in near-wall turbulence, Phil. Trans. R. Soc. A **365**, 647 (2007).

[74] P. Schlatter and R. Örlü, Quantifying the interaction between large and small scales in wall-bounded turbulent flows: A note of caution, Phys. Fluids **22**, 051704 (2010).

[75] R. Mathis, I. Marusic, N. Hutchins, and K. R. Sreenivasan. The relationship between the velocity skewness and the amplitude modulation of the small scale by the large scale in turbulent boundary layers, Phys. Fluids **23**, 121702 (2011).

[76] M. Bernardini and S. Pirozzoli, Inner/outer layer interactions in turbulent boundary layers: A refined measure for the large-scale amplitude modulation mechanism, Phys. Fluids **23**, 061701 (2011).